

ULRR

Two-component lattice Boltzmann model for solute transport in bubbly flows

Item Type	Article
Authors	Byrne, Craig;Shardt, Orest
Citation	Physical Review E, 2025, 111, 035306
Publisher	American Physical Society
Download date	2026-05-13 12:27:17
Item License	https://creativecommons.org/licenses/by-nc-sa/4.0/
Link to Item	https://doi.org/10.34961/researchrepository-ul.29153750

Two-component lattice Boltzmann model for solute transport in bubbly flowsCraig Byrne^{✉*} and Orest Shardt[†]*Bernal Institute and Department of Chemical Sciences, Faculty of Science and Engineering,
University of Limerick, Castletroy, Limerick V94 T9PX, Ireland*

(Received 31 October 2023; accepted 14 February 2025; published 17 March 2025)

A free energy lattice Boltzmann model has been developed to describe a binary system consisting of a nonideal solvent and a gaseous ideal solute. A free energy functional to describe this mixture has been derived, and it is used to determine the driving forces for two lattice Boltzmann equations, one for each component. The well-balanced lattice Boltzmann method is used to avoid discretization errors, which allows correct thermodynamic equilibrium to be achieved for both components as well as high density ratios. In this model, the distribution of the solute between the liquid and vapor phases of the solvent follows Henry's law due to the contributions of the two components to the free energy density. The momenta of the two components are coupled through the use of a mixture velocity in the equilibrium distributions of both components. The model also includes surface tension due to gradients of the solvent density and diffusion due to an added mobility term. The effects of model parameters on phase composition, surface tension, and the rate of solute transport are characterized, with examples of static gas bubbles and flat interfaces demonstrated. Mass transfer of the soluble component in the liquid phase of the nonideal component is characterized, and an equation for the solute diffusion coefficient is provided.

DOI: [10.1103/PhysRevE.111.035306](https://doi.org/10.1103/PhysRevE.111.035306)**I. INTRODUCTION**

Modeling of gas transport in vapor-liquid systems is relevant to understanding processes including oxygenation [1,2], oil and gas extraction [3], bioreactors [4], multiphase reactions [5], carbon dioxide absorption [6,7] from the atmosphere, and hydrogen production [8]. Many of these processes are underpinned by the mechanism of removal/addition of a soluble gas from/into a liquid. Often these processes involve complex geometries of solid-fluid and gas-liquid boundaries, such as deforming bubbles rising in a reactor of curved geometry. In this paper, we derive and present a model for transport of a soluble gas within a solvent that is present in liquid and vapor form.

For several decades, free energy lattice Boltzmann methods have been used to describe flows with multiple phases and components. For example, the free energy lattice Boltzmann method of Swift *et al.* [9] considered two cases: one of a single component in two phases and one of a mixture of two ideal fluids. Recently, Ridl and Wagner [10] extended the single-component multiphase model to multiple components, while other authors have developed models of systems with multiple incompressible fluids [11,12] or used a formulation

based on fugacities [13]. These multicomponent models consider systems with components that are all either nonideal or ideal. One neglected aspect is systems involving a mixture of an ideal and nonideal fluid. Here we consider such a system and describe a model of a binary mixture that consists of a nonideal solvent (present in vapor and liquid phases) and an ideal gas solute (present in the gas phase and dissolved in the liquid phase).

To solve this multicomponent multiphase system, we employ the free energy lattice Boltzmann method (LBM). This method simulates multicomponent and multiphase systems by modification of the single-component lattice Boltzmann (LB) method for an ideal gas [14]. This model employs a diffuse interface [15] approach to describe interfaces between phases. In this approach, the interface is described as a region of finite size in which composition varies continuously between the values in the adjacent phases. This is in contrast to other methods which employ a sharp interface that is tracked with an auxiliary equation or a mesh. Diffuse interface methods are particularly useful for the study of bubbles and droplets undergoing topological changes such as break up or coalescence. The goal of the present paper is to describe mass transfer of multiple components within a framework that is useful for flows with such topological changes.

In general, the exact form of the mass and momentum equations, the coupling between and mass transfer of components, implementation in LB, and the choice of thermodynamic quantities and free energy that are used are application-specific, as each choice has benefits and drawbacks. While initial models were formulated for a single nonideal component (vapor/liquid) or two partially miscible ideal components, a myriad of extensions and reformulations

*Contact author: craig.byrne@ul.ie†Contact author: orest.shardt@ul.ie

have been proposed to describe surfactants [16–19], contact line motion [20], flow in porous media [21,22], and bubble dynamics [23] among other applications [24,25]. Stable simulations with high density ratios were not possible initially, but many solutions have been presented over the years [26–33]. Wagner [26] showed that high-density ratios are possible when the interface is resolved well. However, this approach implies a significant increase in computational demands especially for multicomponent systems in three dimensions. Different solutions come at the cost of solving an additional transport equation, solving an auxiliary equation for pressure [27] or enforcing a constant entropy condition [32]. When one considers multicomponent systems in the lattice Boltzmann framework, previous literature using the free energy formulation tends to focus on different types of mixtures than a nonideal solvent and an ideal gaseous solute. For instance, the surfactant models [16–19] describe a ternary system of a surfactant in a liquid-liquid system. These surfactant models include a coupling between the surfactant and the liquid components which controls the partitioning of the surfactant between the liquid phases. Other researchers have considered mixtures of two nonideal components with a similar coupling. Ridl and Wagner [10] have studied such a system using the free energy lattice Boltzmann method; however, they limited themselves to flat interfaces due to the effects of interface curvature on chemical potentials at equilibrium. Discretization errors also cause discrepancies in the bulk composition values [34] at equilibrium and spurious velocities [35].

One recent advance is the development of the well-balanced free energy lattice Boltzmann method [36]. This method removes discretization artifacts due to the modification of the pressure tensor that resulted in incorrect equilibrium being reached and large spurious velocities. Therefore, it is advantageous to apply this single-component approach to a two-component system to reduce discretization errors and improve the thermodynamic consistency of simulations. A similar approach was taken in the fugacity models of Soomro *et al.* [13], where the well-balanced method is used to solve a binary system described through fugacities for each component. One of the models that was developed by Swift [9] is a binary fluid model with an explicit mobility term. We use this method to introduce variable mass transfer in our two-component model, which to our knowledge has not been implemented in previous work. It is advantageous to include such a diffusion term because the intended practical applications of this model involve mass transfer between vapor and liquid phases.

In the model, formulated below, we describe a binary system of an ideal soluble gas in equilibrium with a nonideal solvent (present as a vapor and liquid). This model is solved using a well-balanced free energy lattice Boltzmann model for two components. The model includes interaction between the two components to control the distribution of the soluble gas between the liquid and vapor phases of the solvent. The model also includes an energy term due to gradients in the density of the nonideal component, which introduces surface tension. This paper combines the well-balanced LBM with a single relaxation time τ_s , which depends on local composition, for both components. This allows proper derivation of a

momentum equation and simulations with different viscosities for the components.

Section II presents the free energy density that we use and its thermodynamic properties. These properties are then used to solve the equations of motion for the mixture using the lattice Boltzmann method, as described in Sec. III. The behavior of the model is demonstrated in Sec. IV. Flat interfaces, bubbles and sinusoidal density distributions are used to show the effects of the model parameters on equilibrium phase compositions, surface tension, and solute mass transfer.

II. MODEL

The binary mixture that we consider is modeled using a free energy of the form

$$F = \int_V \psi(\rho_1, \rho_2, \nabla \rho_1) dV, \quad (1)$$

where the free energy density, ψ , is integrated over the system volume, V . The system is a mixture of a nonideal solvent with density field $\rho_1(\mathbf{x})$ and an ideal gas solute with density field $\rho_2(\mathbf{x})$. When solvent vapor and liquid coexist, we denote the equilibrium compositions of the two phases by (ρ_1^g, ρ_2^g) for the gaseous phase and (ρ_1^l, ρ_2^l) for the liquid phase. The free energy density is made up of the constituent functions

$$\psi = \psi_1(\rho_1) + \psi_2(\rho_2) + \psi_\gamma(\nabla \rho_1) + \psi_{\text{int}}(\rho_1, \rho_2), \quad (2)$$

which are added to incorporate several phenomena. Here ψ_1 is the free energy density of the nonideal component, which can be chosen to give this component an equation of state such as Van der Waals, Peng-Robinson, or Carnahan-Starling. This nonideal fluid will have an interface between its liquid and vapor phases, with the term ψ_γ being used to include the energy of this interface. ψ_2 is the free energy density of the ideal component. Lastly, ψ_{int} describes the interaction between the two components. This term controls the partitioning of the ideal component between the liquid and vapor phases of the nonideal component. From this free energy, the pressure and chemical potentials are derived.

To describe a binary mixture of a nonideal solvent and an ideal gas solute, we prescribe a free energy of the form given by Eqs. (1) and (2). The result is

$$F = \int_V \frac{-8R_1 T (-6\rho_1 + b\rho_1^2)}{(-4 + b\rho_1)^2} + \rho_1 R_1 T \log(\rho_1) - a\rho_1^2 + R_2 T \rho_2 \log(\rho_2) + \frac{\kappa}{2} (\nabla \rho_1)^2 + A\rho_1 \rho_2 dV, \quad (3)$$

where the first three terms give the bulk free energy of the nonideal component, which was chosen to recover the Carnahan-Starling equation of state. The Carnahan-Starling [37–39] equation of state is a modified version of the Van der Waals equation of state where the repulsive term is replaced by the Carnahan-Starling expression for hard spheres [40] and the attraction term is unchanged. The parameter a describes attraction between molecules, while the parameter b describes repulsive interactions. The fourth term recovers an ideal equation of state for the second component. The fifth term describes the free energy of interfaces between phases due to density gradients of the first (nonideal) component. The

system temperature is T , and each component has a gas constant R_i . The κ parameter describes the energy contribution of density gradients, which affects the magnitude of surface tension. The last term describes the interaction between both components, with the strength of the interaction specified by A . An interaction term with this form was also used in surfactant models [16,17].

The form of this free energy is motivated by physical systems of soluble gases in equilibrium with a solvent. Such systems include hydrogen/hydrocarbon [41], hydrogen/water [42], nitrogen/hydrocarbon [43], and nitrogen/alcohol [44]. Taking hydrogen/water as an example, we aim to describe a two-phase system with a gas phase containing hydrogen and water vapor and a liquid phase with water and dissolved hydrogen. At standard conditions, hydrogen can be considered an ideal gas. We consider that this second component has a negligible effect on surface tension. Therefore the interfacial term in the free energy only allows gradients in solvent density to contribute to surface tension.

From the free energy, we can define chemical potentials and a pressure tensor for the system [15]. The free energy functional together with constraints on mass and momentum conservation are used to derive a thermodynamically consistent pressure tensor and chemical potentials. The pressure and chemical potential minimize the free energy at values that satisfy the Gibbs-Duhem relation. The chemical potentials are derived by taking the functional derivatives of Eq. (3) with respect to the compositions. These functional derivatives

$$\mu_1 = \frac{\delta F}{\delta \rho_1}, \quad (4a)$$

$$\mu_2 = \frac{\delta F}{\delta \rho_2} \quad (4b)$$

give the chemical potentials

$$\mu_1 = 16R_1T \left(\frac{-12 + b\rho_1}{(4 + b\rho_1)^3} \right) + R_1T(1 + \log \rho_1) - 2a\rho_1 + A\rho_2 - \kappa \Delta \rho_1, \quad (5a)$$

$$\mu_2 = R_2T \log(\rho_2) + R_2T + A\rho_1. \quad (5b)$$

The isotropic part of the pressure p_0 is also derived from the free energy using

$$p_0 = \rho_1\mu_1 + \rho_2\mu_2 - \psi, \quad (6)$$

and each component's chemical potential to give the expression

$$p_0 = \frac{R_1T\rho_1 \left[1 + \frac{b\rho_1}{4} + \left(\frac{b\rho_1}{4} \right)^2 - \left(\frac{b\rho_1}{4} \right)^3 \right]}{\left(1 - \frac{b\rho_1}{4} \right)^3} - a\rho_1^2 + R_2T\rho_2 - \frac{\kappa}{2}(\partial_\gamma \rho_1)^2 - \kappa \rho_1 \partial_\gamma \partial_\gamma \rho_1 + A\rho_1\rho_2, \quad (7)$$

with summation over repeated Greek indices implied. Away from an interface, the gradient terms in p_0 are zero. We define the bulk pressure to be the sum of the terms in p_0 that do not involve density gradients. Using these quantities derived from the free energy and the fact that minimization of the free energy implies a conserved quantity [15], the pressure tensor can be derived giving

$$P_{\alpha\beta} = p_0\delta_{\alpha\beta} + \kappa(\partial_\alpha \rho_1)(\partial_\beta \rho_1). \quad (8)$$

At equilibrium [45], $\partial_\alpha P_{\beta\alpha} = 0$ and the free energy is minimized. Away from equilibrium, the system is restored by a force given by the Gibbs-Duhem relation

$$F_\beta^{\text{therm}} = -\partial_\alpha P_{\beta\alpha} = -(\rho_1 \partial_\beta \mu_1 + \rho_2 \partial_\beta \mu_2). \quad (9)$$

The component-wise restoring forces are [10]

$$F_{1\alpha} = -\rho_1 \partial_\alpha \mu_1, \quad (10a)$$

$$F_{2\alpha} = -\rho_2 \partial_\alpha \mu_2. \quad (10b)$$

These forces differ from common applications of the free energy lattice Boltzmann method, where a term is included to cancel the gradient of the ideal pressure that is included in conventional LBM. Guo [36] found that in standard approaches this ideal pressure term is not canceled exactly due to discretization error. They suggested a well-balanced approach that introduces a forcing term and modifies the equilibrium distribution to exclude the ideal pressure gradient.

A. Phase composition and surface tension

The parameters of the free energy density determine the compositions of the phases at equilibrium and the tension of the surface between the phases. Due to modeling the solvent with the Carnahan-Starling equation of state, relations for these quantities in terms of the parameters listed above can only be derived in certain ranges and approximations. All model characteristics, however, can be determined numerically.

One can derive approximate solutions [16,46] for the solvent and solute densities in each phase. For the solvent,

$$\rho_1^{g/l} \approx \hat{\rho}_1^{g/l}, \quad (11)$$

where $\hat{\rho}_1^{g/l}$ are the solvent vapor (g) and liquid (l) densities that are found by using the Maxwell construction for the first component's equation of state (assuming no interaction with the other component). This approximation assumes that insufficient solute is present to affect the equilibrium of the dominant component or the interaction is sufficiently weak. It follows that the solvent density ratio is $\phi_1 = \rho_1^l / \rho_1^g = \hat{\rho}_1^l / \hat{\rho}_1^g$.

To derive the equilibrium densities of the solute, we use the fact that the solute chemical potential [Eq. (5b)] is equal in both phases at equilibrium:

$$\mu_2(\rho_1^l, \rho_2^l) = \mu_2(\rho_1^g, \rho_2^g), \quad (12)$$

with the interfacial term $\kappa \Delta \rho_1$ being zero in the bulk. It follows that the solute density ratio $\phi_2 = \rho_2^l / \rho_2^g$ and Henry's constant H are

$$H = \phi_2 = \frac{\rho_2^l}{\rho_2^g} = \exp\left(-\frac{A(\rho_1^l - \rho_1^g)}{R_2T}\right). \quad (13)$$

When $\rho_1^l \gg \rho_1^g$, this simplifies to

$$H = \frac{\rho_2^l}{\rho_2^g} = \exp\left(-\frac{A\rho_1^l}{R_2T}\right). \quad (14)$$

If the midpoint of the solute densities in the vapor and liquid phases is ρ_2^0 , the solute densities in both phases can be expressed as deviations from this midpoint:

$$\rho_2^{g/l} = \rho_2^0(1 \pm \delta\rho_2). \quad (15)$$

Using Eq. (13), it follows that

$$\delta\rho_2 = \tanh\left(\frac{A(\rho_1^g - \rho_1^l)}{2R_2T}\right). \quad (16)$$

We verify in Sec. IV that the chemical potentials and bulk pressures are equal in both phases at equilibrium. When choosing parameters for simulations, we focus on conditions that satisfy

$$\rho_1^l \gg \rho_2^g \approx \rho_1^g > \rho_2^l, \quad (17)$$

which represents a typical system such as hydrogen bubbles in water.

The surface tension σ can be determined by integrating the normal and tangential parts of the pressure tensor (7) across an interface. However, this requires a solution for the density profiles of all components. We therefore use numerical integration of a simulated solution and compare this value with the value found by fitting the Young-Laplace equation for bubbles with varying radii.

III. IMPLEMENTATION WITH THE LATTICE BOLTZMANN METHOD

The lattice Boltzmann method solves the Navier-Stokes equations by using a discretized form of the Boltzmann equation, called the lattice Boltzmann equation (LBE) for a gas. The LBE describes the evolution of populations that move between the nodes of a lattice. Macroscopic quantities, such as density and velocity, are obtained from the moments of these populations. Collisions between gas molecules are modeled by relaxation of the populations towards an equilibrium distribution. Originally, LBM was formulated for a single ideal component, but various extensions to multicomponent and multiphase systems have been proposed. Solving the LBE is equivalent to solving the macroscopic Navier-Stokes equations in the hydrodynamic limit. The macroscopic scale equations for a lattice Boltzmann scheme can be derived by Chapman-Enskog (or other) expansion [14]. A more detailed overview of the LBM can be found in a variety of sources [14,47].

To solve the transport equations for the system, the well-balanced [36] formulation of the free energy lattice Boltzmann method [9] is employed, where the LBE is solved incorporating the free energy model described above. For the solute-solvent system, we use two LBEs, one for the solvent ρ_1 and another for the solute ρ_2 given respectively by

$$\begin{aligned} & g_i(\mathbf{x} + \mathbf{c}_i\Delta t, t + \Delta t) - g_i(\mathbf{x}, t) \\ &= -\frac{\Delta t}{\tau_s} [g_i(\mathbf{x}, t) - g_i^{\text{eq}}(\mathbf{x}, t)] + \left(1 - \frac{\Delta t}{2\tau_s}\right) G_i(\mathbf{x}, t)\Delta t, \end{aligned} \quad (18a)$$

$$\begin{aligned} & h_i(\mathbf{x} + \mathbf{c}_i\Delta t, t + \Delta t) - h_i(\mathbf{x}, t) \\ &= -\frac{\Delta t}{\tau_s} [h_i(\mathbf{x}, t) - h_i^{\text{eq}}(\mathbf{x}, t)] + \left(1 - \frac{\Delta t}{2\tau_s}\right) H_i(\mathbf{x}, t)\Delta t, \end{aligned} \quad (18b)$$

where g_i is the solvent population distribution, and h_i is the solute population distribution. Forces are included in the LBE by

source terms, with G_i and H_i being the solute and solvent forcing terms, respectively. The first terms on the right-hand sides of these equations are the commonly used Bhatnagar-Gross-Krook (BGK) collision operator [14] for each component, where the viscosity of the mixture [48,49] is related to τ_s by

$$v = c_s^2 \left(\tau_s - \frac{\Delta t}{2} \right) = \frac{\rho_1 v_1 + \rho_2 v_2}{\rho}. \quad (19)$$

Here we are using a mixture viscosity that is the mass-weighted average of the individual components' viscosities, v_1 and v_2 . $c_s^2 = 1/3$ is the isothermal lattice speed of sound. If the components have different viscosities, the value of the mixture relaxation time varies according to the local composition.

The LBE is a discretization of the continuous Boltzmann equation. Upon discretization, the LBE refers to a fixed grid of fluid nodes with populations, g_i and h_i , moving at m discrete velocities \mathbf{c}_i with $i = 0, 1, 2, \dots, m-1$ between the nodes. Commonly lattices are classified by their spatial dimension, n and discrete velocity set, m , as a DnQm lattice. The LBE is then evolved in time through a process of streaming, captured by the left-hand side of Eqs. (18a) and (18b). Streaming refers to the motion of populations to adjacent nodes under their velocity \mathbf{c}_i . Followed by this is collision, which is captured by the right-hand sides of the equations. Collision refers to these streamed populations colliding and relaxing to the equilibrium distributions g_i^{eq} and h_i^{eq} . This process of streaming and collision is repeated until reaching the required amount of time steps for a simulation.

To relate the population distributions to macroscopic fluid quantities, we define moments of the populations. These moments are given by

$$\rho_1 = \sum_i g_i, \quad \rho_1 u_{1\alpha} = \sum_i g_i c_{i\alpha} + \frac{(F_{1\alpha} + \Gamma_2 \partial_\alpha \mu_2) \Delta t}{2\rho_1}, \quad (20)$$

for the solvent and

$$\rho_2 = \sum_i h_i, \quad \rho_2 u_{2\alpha} = \sum_i h_i c_{i\alpha} + \frac{(F_{2\alpha} + \Gamma_1 \partial_\alpha \mu_1) \Delta t}{2\rho_2}, \quad (21)$$

for the solute. Here ρ_1 and ρ_2 are the macroscopic solvent and solute densities, respectively. Due to applying the modified [36] forcing method of Guo [50], the velocity must be redefined due to the applied forces. The component velocities $u_{1\alpha}$ and $u_{2\alpha}$ are used to calculate a mixture velocity u_α according to $u_\alpha = \frac{u_{1\alpha}\rho_1 + u_{2\alpha}\rho_2}{\rho_1 + \rho_2}$. This mixture velocity u_α is used as the velocity in the calculation of the equilibrium populations to which g_i and h_i relax. The use of a mixture velocity in the equilibrium distributions of both components ensures that over time both components move with a common velocity. The equilibrium distributions are given by

$$\begin{aligned} g_i^{\text{eq}} &= w_i \rho_1 \left(\frac{\Gamma_1 \mu_1}{c_s^2 \rho_1} + \frac{c_{i\alpha} u_\alpha}{c_s^2} + \frac{u_\alpha u_\beta (c_{i\alpha} c_{i\beta} - c_s^2 \delta_{\alpha\beta})}{2c_s^4} \right) \\ & i = 1, 2, \dots, m-1, \end{aligned} \quad (22a)$$

$$g_0^{\text{eq}} = \rho_1 - \sum_{i=1}^{m-1} g_i^{\text{eq}} \quad (22b)$$

and

$$h_i^{\text{eq}} = w_i \rho_2 \left(\frac{\Gamma_2 \mu_2}{c_s^2 \rho_2} + \frac{c_{i\alpha} u_\alpha}{c_s^2} + \frac{u_\alpha u_\beta (c_{i\alpha} c_{i\beta} - c_s^2 \delta_{\alpha\beta})}{2c_s^4} \right) \quad (23a)$$

$$i = 1, 2, \dots, m-1,$$

$$h_0^{\text{eq}} = \rho_2 - \sum_{i=1}^{m-1} h_i^{\text{eq}}. \quad (23b)$$

These equilibrium distributions differ from those of the conventional LBM due to our use of the well-balanced approach and by incorporation of the mobility terms containing the mobility parameters Γ_1 and Γ_2 . As derived in Appendix A, mass equations (A20) show that these mobility parameters lead to mobility coefficients $M_j = (\tau_s - \frac{\Delta t}{2})\Gamma_j$ for each component. We take a similar approach to Guo [36] and set the constants in the equilibrium as zero. The zeroth populations g_0^{eq} and h_0^{eq} are calculated differently, and conservation of mass is exploited to calculate their values.

Inclusion of these terms in the equilibrium leads to second moments given by

$$\sum_i g_i^{\text{eq}} c_{i\alpha} c_{i\beta} = \rho_1 u_\alpha u_\beta + (\Gamma_1 \mu_1) \delta_{\alpha\beta}, \quad (24a)$$

$$\sum_i h_i^{\text{eq}} c_{i\alpha} c_{i\beta} = \rho_2 u_\alpha u_\beta + (\Gamma_2 \mu_2) \delta_{\alpha\beta}, \quad (24b)$$

which result in diffusion terms in the mass equations for both components. The term that is responsible for the ideal pressure of the fluid in conventional LBM has also been removed. This has the effect of changing the second moments of g_i and h_i in comparison to the standard methods. To solve the proper Navier-Stokes equations, the removed terms are added to the forcing terms G_i and H_i . These forcing terms are given by

$$G_i = w_i \rho_1 \left[\frac{c_{i\alpha} (F_{1\alpha} + \Gamma_2 \partial_\alpha \mu_2)}{c_s^2} + \frac{u_\alpha (F_{1\beta} + \Gamma_2 \partial_\beta \mu_2 + c_s^2 \partial_\beta \rho_1) (c_{i\alpha} c_{i\beta} - c_s^2 \delta_{\alpha\beta})}{c_s^4} + \frac{1}{2} \left(\frac{c_{i\gamma}^2}{c_s^2} - 2 \right) (u_\gamma \partial_\gamma \rho_1) \right] \quad (25)$$

and

$$H_i = w_i \rho_2 \left[\frac{c_{i\alpha} (F_{2\alpha} + \Gamma_1 \partial_\alpha \mu_1)}{c_s^2} + \frac{u_\alpha (F_{2\beta} + \Gamma_1 \partial_\beta \mu_1 + c_s^2 \partial_\beta \rho_2) (c_{i\alpha} c_{i\beta} - c_s^2 \delta_{\alpha\beta})}{c_s^4} + \frac{1}{2} \left(\frac{c_{i\gamma}^2}{c_s^2} - 2 \right) (u_\gamma \partial_\gamma \rho_2) \right]. \quad (26)$$

The equilibrium distributions and the first moments of each population in Eq. (20) and Eq. (21) contain mobility related contributions from the other component: $\Gamma_2 \partial_\alpha \mu_2$ for the solvent and $\Gamma_1 \partial_\alpha \mu_1$ for the solute. This is equivalent to applying these terms as forces. They are written explicitly as they are necessary to cancel mobility related errors when deriving the

total momentum equation in the Chapman-Enskog analysis as provided in Appendix A.

The equilibrium distributions are derived such that they satisfy the following moment equations, with the first nonzero moments being

$$F_{1\alpha} = \sum_i G_i c_{i\alpha},$$

$$\sum_i G_i c_{i\alpha} c_{i\beta} = c_s^2 (u_\beta \partial_\alpha \rho_1 + \rho_1 \partial_\alpha u_\beta + u_\gamma \partial_\gamma \rho_1 \delta_{\alpha\beta}) + F_{1\alpha} u_\beta + F_{1\beta} u_\alpha \quad (27)$$

and

$$F_{2\alpha} = \sum_i H_i c_{i\alpha},$$

$$\sum_i H_i c_{i\alpha} c_{i\beta} = c_s^2 (u_\beta \partial_\alpha \rho_2 + \rho_2 \partial_\alpha u_\beta + u_\gamma \partial_\gamma \rho_2 \delta_{\alpha\beta}) + F_{2\alpha} u_\beta + F_{2\beta} u_\alpha. \quad (28)$$

These terms incorporate the forces on the solvent $F_{1\alpha}$ and solute $F_{2\alpha}$ from Eq. (10a) and Eq. (10b) into the LBE.

The lattice weights w_i are dependent on the type of DnQm lattice the LBEs are being solved in. Fourth-order stencils [51,52] are used to evaluate the gradient and Laplacian terms to solve the pressure and chemical potentials.

With the LBEs, moments, and equilibrium distributions, equations of motion for the system can be derived using the Chapman-Enskog [14,36] expansion. With this method, the LBE is expanded under a Taylor series, with the resulting derivatives and populations expanded by order of the Knudsen number ϵ . The resulting expansions can be brought to the desired hydrodynamic and numerical limit resulting in equations of motion that are solved by the system's LBE. Based on the Chapman-Enskog analysis of the LBEs in Appendix A, the total momentum equation is

$$\partial_t (\rho \mathbf{u}) + \nabla \cdot (\rho \mathbf{u} \mathbf{u}) = -\rho_1 \nabla \mu_1 - \rho_2 \nabla \mu_2 + \nabla \cdot \{ \nu \rho [\nabla \mathbf{u} + \nabla \mathbf{u}^T + (\nabla \cdot \mathbf{u}) \mathbf{I}] + \nu \mathbf{E}_2 \}, \quad (29)$$

and the mass equations for each component are given by

$$\partial_t \rho_1 + \nabla \cdot (\rho_1 \mathbf{u}) = \nabla \cdot (M_1 \nabla \mu_1 - M_2 \nabla \mu_2) + \nabla \cdot \mathbf{e}_1(\rho_1, \mathbf{u}), \quad (30a)$$

$$\partial_t \rho_2 + \nabla \cdot (\rho_2 \mathbf{u}) = \nabla \cdot (M_2 \nabla \mu_2 - M_1 \nabla \mu_1) + \nabla \cdot \mathbf{e}_1(\rho_2, \mathbf{u}), \quad (30b)$$

with the sum of the component mass equations giving the total mass equation of the mixture. There are error terms in the recovered Navier-Stokes equations. The details of the error expressions are provided in Appendix A. The diffusion of chemical potential terms in the mass equations have errors $e_1(\rho_j, \mathbf{u})$ given by (A21), the total mass equation has an error given by (A22), and the momentum equation has the error term \mathbf{E}_2 given by (A33). We also note that similar error terms are found in the component mass equations of Swift's binary model [9] when diffusive terms were considered. The spurious velocities in our model are shown later to be small as in other well-balanced approaches.

IV. RESULTS AND DISCUSSION

Here simulations using the model are presented, with demonstrations of both interface profiles and static bubbles. Simulations with flat interfaces are used to characterize the composition of the phases. Demonstrations are first presented with the intention to show that the model can in fact reach the expected equilibrium. With this established, the effects of coupling both components are investigated by varying the interaction parameter A at different conditions. We show that the computed phase compositions match the expected values given previously. Simulations of bubbles are used to investigate surface tension. Young-Laplace tests are first used to determine the surface tension coefficient; they are then used to show how the surface tension is affected by the interaction term. In the last section, the mass transfer characteristics are shown with calculations of the mobility coefficients and comparison with expected values.

A. Method and parameters

The basic steps of the lattice Boltzmann algorithm which solves the LBEs given by Eq. (18a) and Eq. (18b) are as follows. First, an initial density and momentum distribution for each component is used to calculate the initial population values by using the equilibrium distribution given by Eq. (22a) and Eq. (23a). These initial populations are then streamed and collided, with streaming captured by the left-hand side of the LBE and performed by a simple copy operation. The moments of the streamed populations are used to calculate new macroscopic quantities such as density and momentum. Collision is captured by the right-hand side of the LBEs and is a simple arithmetic operation; at every time step before collision the moments of the streamed populations are used to calculate new equilibrium populations. The forces in the G_i and H_i source terms are evaluated using the Laplacian and gradient stencils. This process is repeated until the required final time step from which macroscopic fluid quantities are derived.

All simulations are two-dimensional with nine discrete velocities, which corresponds to using a D2Q9 lattice with its corresponding weights w_i and discrete velocity vector components $c_{i\alpha}$. The simulations were written in the Julia programming language and accelerated on an NVIDIA Geforce 4070 Ti Graphics Processing Unit (GPU) using the CUDA.jl [53] package, as the lattice Boltzmann algorithm is amenable to high parallelism and simple to implement on a GPU. The NVIDIA Tesla V100 GPUs of the Irish Centre for High-End Computing (ICHEC) and MeluXina.

In the subsequent sections, different flat interfaces, bubbles, and sinusoids are simulated with the purpose of determining how key model characteristics are related to the model parameters. These model characteristics are the surface tension σ , solute density ratio H , and solute mobility coefficient M_2 . These characteristics broadly describe the binary model macroscopically. While the bulk compositions can be determined approximately, theoretical determination of the other parameters is more difficult for a nonideal equation of state. However, one can determine these properties by simulation. For the GPU-accelerated code used here, 100 000 time

steps on a 160×160 lattice took under a minute to complete. Therefore running smaller tests to determine system parameters for larger simulations is a viable and practical option using modern hardware.

It is useful to characterize the nonideal solvent in terms of its critical properties: critical density $\rho_c = 0.5218/b$, critical pressure $p_c = a(0.3773^2)0.4963/b^2$, and critical temperature $T_c = 0.3773a/bR_1$. For all simulations, we use the numerical values $\rho_c = 3.5$, $R_1 = 1$, and $T = T_r T_c$, where T_r is the reduced temperature. Two sets of reduced temperature and critical pressure values are used throughout; the higher temperature values are $T_r = 0.92$ and $p_c = 0.01$, and the lower temperature values are $T_r = 0.5$ and $p_c = 0.001$. The Maxwell construction is used with the above parameters for the single-component Carnahan-Starling equation to give initial densities for both sets of simulations. For example, the high temperature gives $\rho_1^l = 6.287$ and $\rho_1^g = 1.425$. The solute parameters are set such that $R_2 = R_1$, and the initial average amount of solute is $\rho_2^0 = 1.0$ for the higher temperature and $\rho_2^0 = 0.015$ for the lower temperature. The kinematic viscosities are $\nu_1 = 0.133$ and $\nu_2 = 0.033$, which are used in the calculation of τ_s . The mobility constants are set to $\Gamma_1 = \Gamma_2 = 0.5$ for all simulations with the exception of the results shown in Fig. 10 where $\Gamma_1 = \Gamma_2 = 0.1$ and in the last section where the mobility is varied. These parameters are used for all simulations except where explicitly stated otherwise. The remaining parameters A and κ are adjusted to show the effects of the interaction and interfacial terms.

All the tests are performed with a domain size $(N_x, N_y) = (160, 160)$ with the exception of the results shown in Figs. 2 to 7, 9, and 10. Figures 2 to 7 are computed with an odd domain of $(N_x, N_y) = (165, 165)$; Figs. 9 and 10 are computed with a domain of $(N_x, N_y) = (1600, 6)$. The results in Sec. IV D have domain sizes of $(N_x, N_y) = (80, 80)$. The domain has periodic boundaries, and a uniform spacing ($\Delta x = \Delta y = 1$) is used. In the simulations with a gas bubble, all bubbles were centered at $x = \frac{N_x}{2}$ and $y = \frac{N_y}{2}$ or the nearest integer rounded down. The studies of the interface profiles and mobility are one-dimensional in x , but the same domain size is used in the y direction. These cases are initialized by repeating the same profiles throughout the y dimension. Due to the periodic boundary conditions, two interfaces were simulated with one at $x = \frac{N_x}{4}$ and one at $x = \frac{3N_x}{4}$. The sinusoid that was used for the diffusion simulations had one period of the solute density distribution across the domain with its maximum at $x = \frac{N_x}{4}$ and minimum at $x = \frac{3N_x}{4}$.

B. Flat interfaces

For a flat interface, we first demonstrate an initially uniform solute separating into both phases of the solvent. The solute is initialized flat at a density of $\rho_2(x) = \rho_2^0 = 0.0012$. The initial density of the solvent is found through Maxwell reconstruction of the single-component form of Eq. (7), and the solvent profile is initialized using an approximate tanh profile. The initial and steady state profiles are shown in Fig. 1. It can be seen that the solute partitions into liquid and vapor phases. The densities in each phase partition according to the relation (17), with the average solute density being of the order of the solvent vapor density.

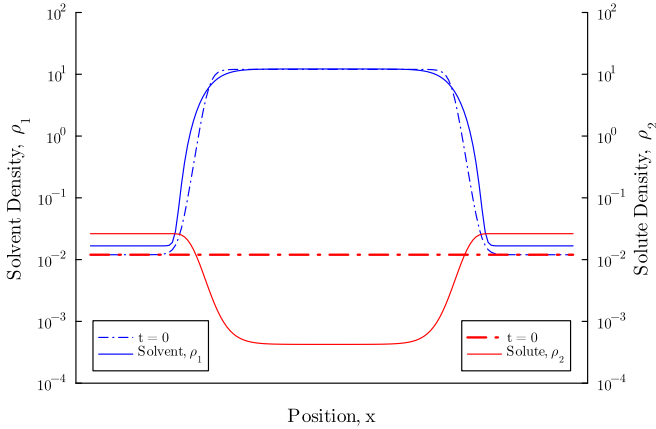


FIG. 1. Final (solid) and initial (dash-dot) density profiles at $y = 51$ with $T_r = 0.5$, $A = 0.000135$, $p_c = 0.001$, and $\kappa = 0.008$.

To show the effects of varying the interaction parameter A on the equilibrium distribution of each component, their chemical potentials, the pressure distribution of the mixture and flat interfaces were simulated for a range of A . The interface profiles are initialized using approximate tanh profiles based on the solutions for density in Sec. II A. The bulk density of the solute was found using Eq. (16). The solvent densities were found through the Maxwell construction for the solvent's equation of state. It should also be noted that for even a single-component liquid/vapor system, the relation Eq. (9) holding is not guaranteed [45] in the discrete case. To check for thermodynamic consistency, it is prudent to verify equality between both phases of the total pressure and chemical potentials at the end of a simulation. If equality can be reached, it shows the thermodynamic consistency of the computed solution. Therefore, simulations were run to $t = 2 \times 10^7$ time steps to allow both phases to reach equilibrium, and the chemical potentials of each component and the bulk pressure were calculated.

The density profiles of the solvent and solute for several values of the interaction parameter A are shown in Fig. 2. In these simulations, the higher temperature parameters are

used, and the domain size is $N_x = N_y = 165$. Odd domain dimensions are used to suppress instabilities seen in domains with even dimensions. This figure shows that varying the interaction parameter elicits a small change in the bulk compositions of the solvent. For the solute, A is shown to affect the partitioning of the solute between the liquid and vapor phase. This is consistent with the observed effects of including a similar interaction term in surfactant models [16,17]. The inclusion of this interaction term affects both bulk compositions and surface tension [46]. The pressure and chemical potentials were found using Eq. (8), (5a), and (5b), and they are shown in Figs. 3 and 4. Deviations of the chemical potentials and pressures from the values in the bulk are shown in these figures. The pressures and chemical potentials are equal between the phases, indicating that the system had reached thermodynamic equilibrium for all values of A . Variation in the pressure near an interface is due to the thinness of the interface, with an increase in A causing the interface width to shrink slightly. The chemical potentials are flat to near machine precision in the bulk and interface regions. Figure 4 shows that the pressure tensor component P_{xx} is also flat through both interfaces.

For the cases in Figs. 2, 3, and 4, once A is increased such that $H^{-1} = \rho_2^g / \rho_2^l$ is of the order of the solvent density ratio ϕ_1 , the bulk compositions of the solvent are changed. When the densities of both components are similar in the gas phase, the solvent composition changes will be negligible so long as $H^{-1} \ll \rho_1^g / \rho_1^s$. This condition is satisfied by common substances at typical ambient conditions. For example, the density ratio of water is $\phi_1 \sim 10^5$ at 10°C and $\phi_1 \sim 10^3$ near 100°C , whereas for common gases, such as hydrogen, oxygen, and nitrogen, the Henry's constant [54] is $H \sim 10^{-2}$.

The lower temperature set is more suited to these conditions. At this lower temperature, the solvent density ratio is higher and Henry's law constant is lower. Accordingly, interface profiles were computed at the lower reduced temperature. Initial simulation parameters were calculated in the same manner as the previous cases, and the simulations were run to a longer time of $t = 4 \times 10^7$ time steps to allow equilibrium to be reached. The equilibrium compositions, chemical potentials, and pressure are shown in Figs. 5, 6, and 7. With these parameter values, the density ratio of the solvent is $\phi = 723$.

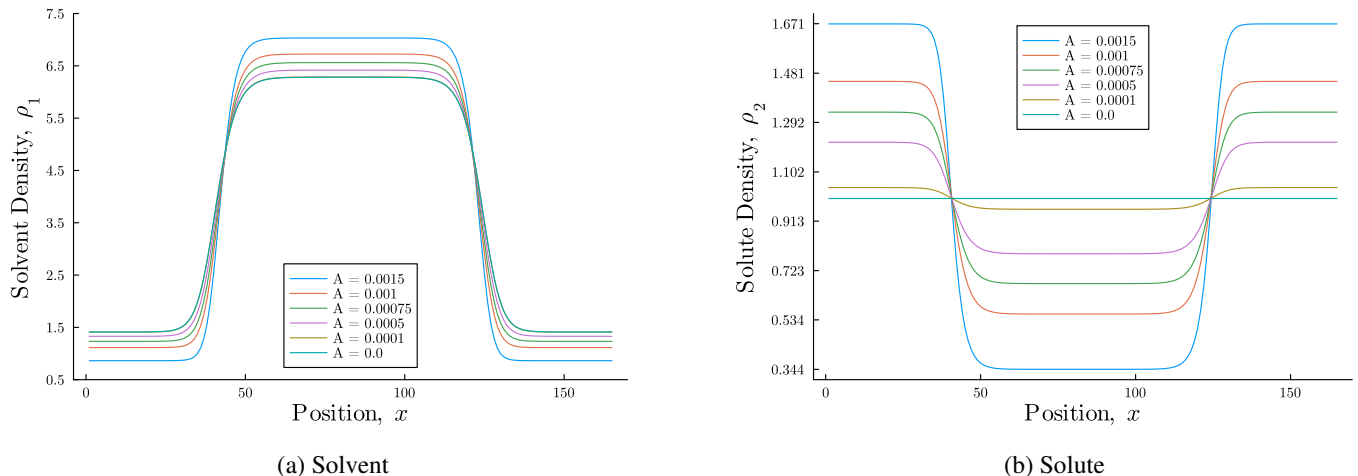


FIG. 2. Equilibrium density profiles at $y = 51$ with $\kappa = 0.008$, $p_c = 0.01$, $T_r = 0.92$, and $A \in \{0.0015, 0.001, 0.00075, 0.0005, 0.0001, 0\}$.

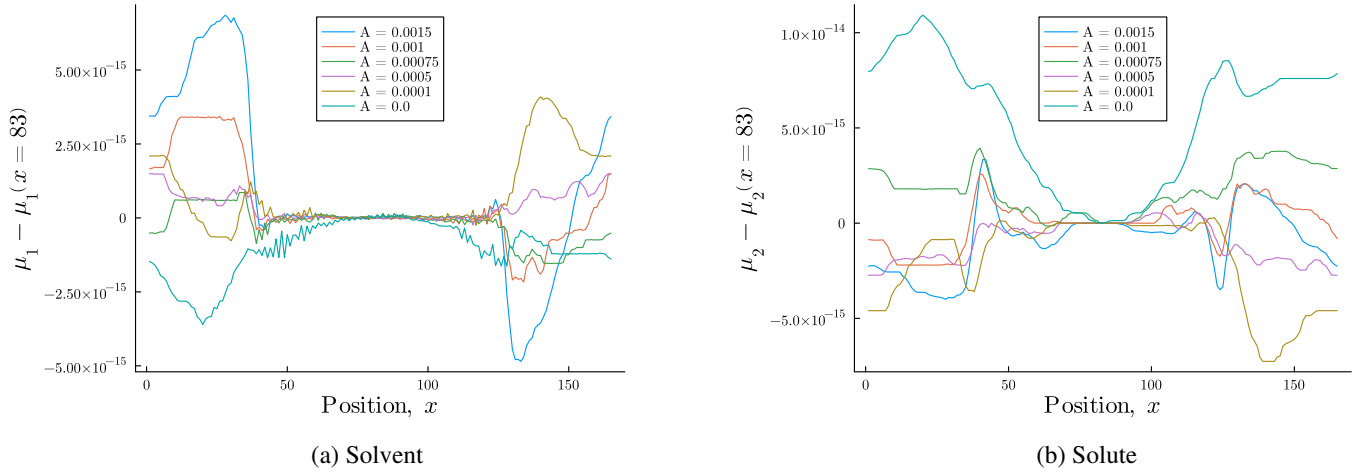


FIG. 3. Deviations of the chemical potentials from their values in the bulk at $y = 51$ with $\kappa = 0.008$, $p_c = 0.01$, $T_r = 0.92$, and $A \in \{0.0015, 0.001, 0.00075, 0.0005, 0.0001, 0\}$.

The bulk compositions of the solvent at this lower reduced temperature remain essentially independent of A ; compare Fig. 5 and Fig. 2. The chosen values of A give a range of Henry’s constants from $H = 1/62.5$ to $H = 1$, and this can be seen from Fig. 2, with $A = 0$ giving a uniform solute density profile. The chemical potentials are uniform at equilibrium, and the pressure is equal in both phases. At this high density ratio, slight fluctuations in the pressure tensor component P_{xx} are evident in the interfacial regions. Therefore, it is clear that the current model is able to reach high solvent density ratios and low Henry’s constants as in common systems at ambient conditions. It is also evident that the system can reach true thermodynamic equilibrium with the variations in chemical potential being near machine precision in both cases.

To demonstrate how the solute is distributed between the two phases, multiple flat interfaces with different average solute densities $\rho_2^0 \in \{0.005, 0.01, 0.02, 0.04, 0.05\}$ were simulated for $A \in \{0.000135, 0.0001, 0.00008\}$. For all cases the lower temperature is used, $T_r = 0.5$ with $\kappa = 0.008$ and $p_c = 0.001$. The initial density of the solvent is again found through the Maxwell construction for the single-component

form of Eq. (7). The density profiles were initialized using approximate tanh profiles. The simulations ran for $t = 1 \times 10^7$ time steps. The amount of solute in each phase was shown to have a linear relationship, with the slope giving Henry’s constant. These results are shown in Fig. 8. In the resulting equilibrium density distributions, the solute distributes between the two phases according to the interaction strength A , which determines Henry’s constant. Clearly, this value is independent of the average amount of solute in the system. While the solvent takes on specific composition values due to the parameters ρ_c and T_r , the equilibrium solute densities in each phase depend on Henry’s constant (set by the interaction parameter A), the gas constant R_2 , the temperature T , and the solvent densities in each phase.

When adjusting T_c , p_c , or κ , some parameter values will give too small an interface width, ξ . When the interface spans less than three computational grid points, lack of resolution affects the calculations of the gradient and Laplacian terms in the solvent partial pressure and equilibrium distributions. However, the interface width can be easily adjusted by varying p_c and κ while keeping other parameters constant. This results in interfaces with increasing interface width at the same density ratio of each component for the system, if the reduced temperature is kept the same.

Phase compositions were also determined for a wide range of temperatures. To test the maximum solvent density ratio that could be obtained with the model, simulations were run with $p_c = 0.001$ and $\kappa = 0.008$. Two values of A are tested: $A = 0.000135$ for Fig. 9 and $A = 0.00006$ for Fig. 10. The first case corresponds to a maximum predicted $H \approx 1/6$ while the second corresponds to $H \approx 1/62$, both for a predicted solvent density ratio of $\phi \approx 700$. Accordingly, the first case is referred to as the high H case, while the second is the low H case. The system temperature, T , is varied between a $T_r = 0.5$ and 0.92 . Interface profiles are then computed at each temperature until they reach equilibrium, which is determined by verifying that the bulk pressure is equal in the two phases. The resulting bulk densities at each temperature are recorded from each interface profile.

In Figs. 9 and 10, the computed solute phase diagrams are compared with an *a priori* estimation of the solute

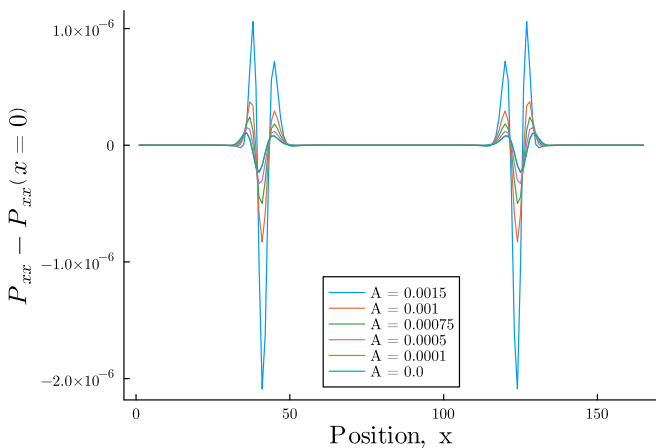


FIG. 4. Deviations in pressure P_{xx} from the bulk values across flat interfaces at $y = 51$ with $\kappa = 0.008$, $p_c = 0.01$, $T_r = 0.92$, and $A \in \{0.0015, 0.001, 0.00075, 0.0005, 0.0001, 0\}$.

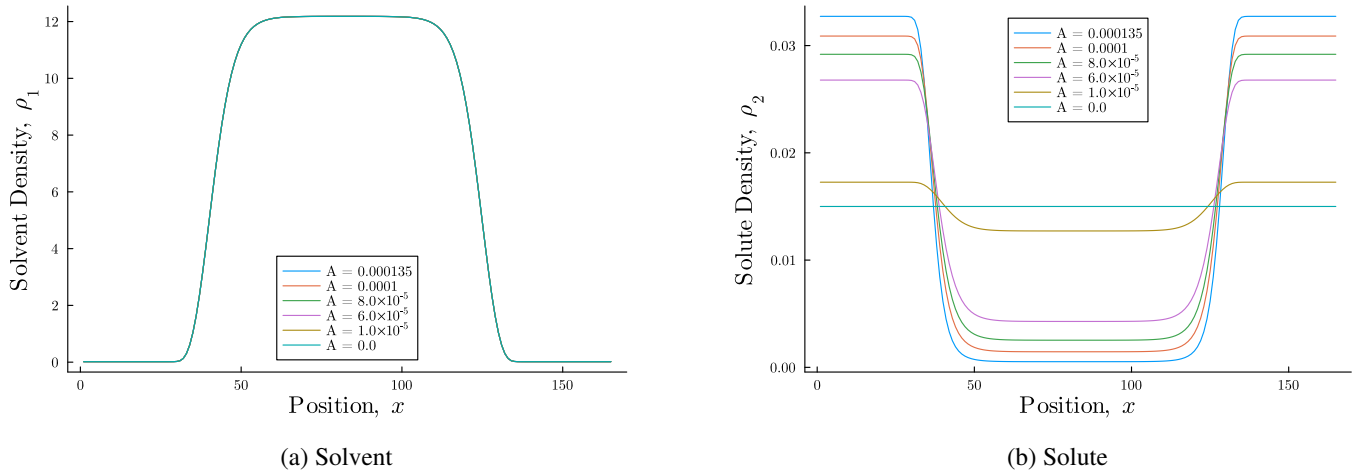


FIG. 5. Equilibrium density profiles at $y = 51$ with $\kappa = 0.008$, $p_c = 0.001$, $T_r = 0.5$, and $A \in \{0.00001, 0.00006, 0.00008, 0.0001, 0.000135\}$.

composition. The estimate uses the average initial amount of solute in the domain ($\rho_2^0 = 0.015$) for the calculation of the compositions by Eq. (16). The computed results deviate slightly from these estimate value. The reason for the difference between these values is the excess solute in the interfacial region, which is not accounted for in the preceding analysis of bulk behavior. With increasing domain size, the fraction of the total area occupied by the diffuse interface decreases, and the simulated values converge to the estimated values. For both cases, the solvent follows the single-component Carnahan-Starling equation of state almost exactly, which is consistent with our assumption that the solvent is unaffected by the presence of solute.

It is interesting to note that in the low H case, the solute densities start to mimic the form of the solvent equation of state. The low H case corresponds to a strong interaction between both components, and the solute densities vary nonlinearly with temperature, unlike the high H case. The maximum simulated density ratio was $\phi_1 = 729$ with $\rho_1^l = 12.18$ and $\rho_1^g = 0.0167$ for the solvent with a Henry's law

constant of $H = 1/62.528$ for the solute. These cases are shown by the bottom symbols in Fig. 10.

C. Bubbles

This section demonstrates the characteristics of surface tension for gas bubbles in the solute-solvent model. We simulate both the high and low temperatures to demonstrate the nature of surface tension near and far from the critical point. Surface tension values are calculated from the Young-Laplace equation, and the values are compared with a secondary calculation of surface tension by integration of the pressure tensor across an interface.

We first demonstrate the ideal component phase separating from an initially uniform distribution as was done for the flat interface case in Fig. 1. In Fig. 11 a gas bubble was simulated centered at $x = 80$, $y = 80$, with parameters set at $\kappa = 0.008$, $T_r = 0.92$, $p_c = 0.01$, and $A = 0.001$. The simulation was run to 1×10^7 time steps at which time the chemical potentials were equal. Due to the circular interface, there was a slight

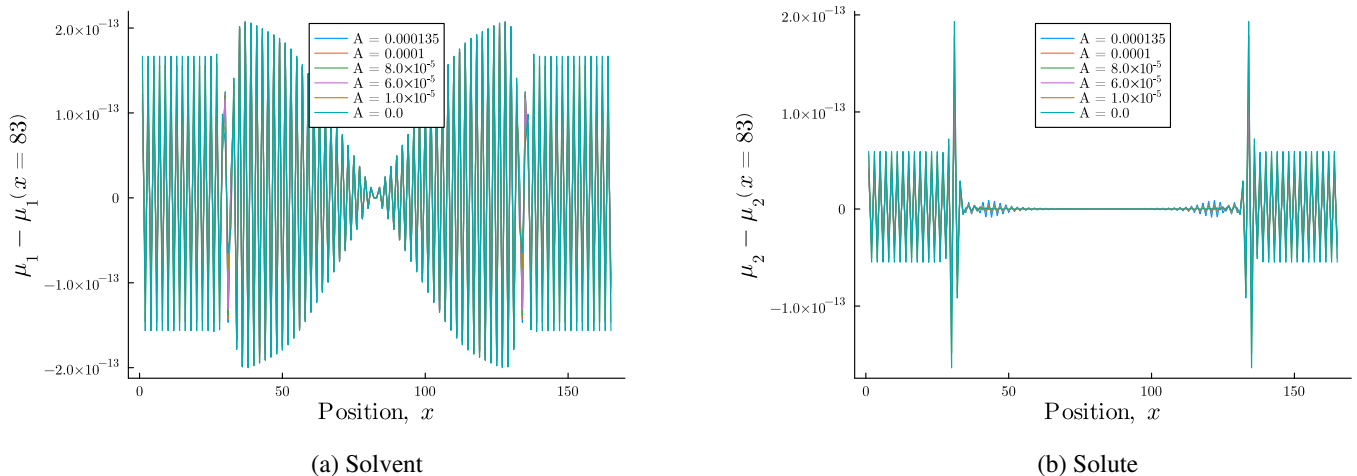


FIG. 6. Deviations of the chemical potentials from their values in the bulk at $y = 51$ with $\kappa = 0.008$, $p_c = 0.001$, $T_r = 0.5$, and $A \in \{0.00001, 0.00006, 0.00008, 0.0001, 0.000135\}$.

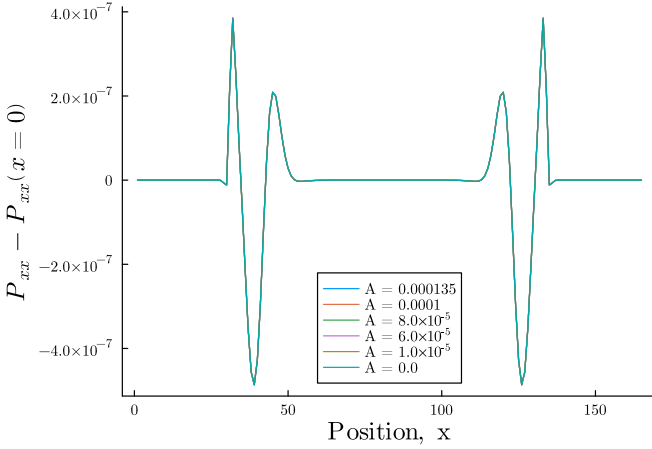


FIG. 7. Deviations in pressure P_{xx} from the bulk values across flat interfaces at $y = 51$ with $\kappa = 0.008$, $p_c = 0.001$, $T_r = 0.5$, and $A \in \{0.00001, 0.00006, 0.00008, 0.0001, 0.000135\}$.

pressure difference between the inside and outside of the bubble. As in the one-dimensional (flat interface) case, the initially uniform solute density distribution phase separates according to the specified free energy.

Multiple gas bubbles with different radii were computed until they reached equilibrium. The radii R and the differences in pressure Δp between the phases were computed, and the slope of the linear fit gives the surface tension as per the Young-Laplace law, $\Delta p = \frac{\sigma}{R}$. The pressure is calculated using Eq. (7). The value of κ was varied to demonstrate different surface tensions. The gas bubbles were initialized with radii of $R_0 \in \{25, 28, 30, 32, 34\}$ for both high- and low-temperature sets. Three cases were simulated for the high- and low-temperature values: $\kappa = [0.008, 0.004, 0.001]$ was used for the high-temperature set and $\kappa \in \{0.008, 0.006, 0.004\}$ for

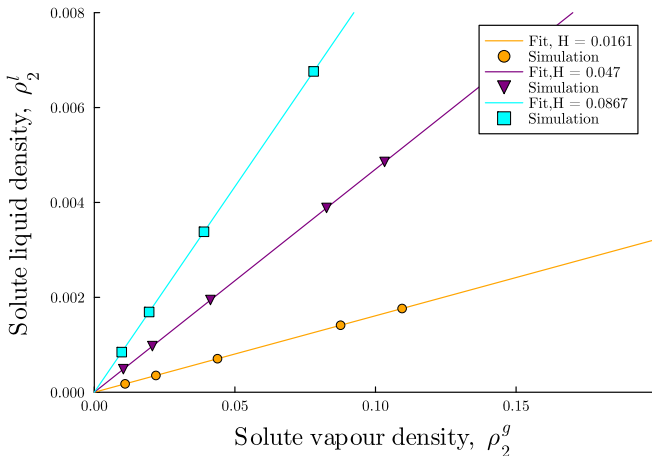


FIG. 8. Distribution of solute in the vapor and liquid phases for varying amounts of solute and different values of A . Symbols show simulation results and the lines were fitted to determine Henry's constant for $A = 0.000135$, $H = 1/62.1$ (cyan), $A = 0.0001$, $H = 1/21.27$ (purple), and $A = 0.00008$, $H = 1/11.53$ (yellow). For all cases, $\kappa = 0.008$, $T_r = 0.5$, and $p_c = 0.001$. The theoretical Henry's constants (Eq. (13)) for these cases are $1/62$, $1/21.3$, and $1/11.5$, respectively.

the low-temperature set. For the high-temperature value, the critical pressure was $p_c = 0.01$ and the interaction parameter was $A = 0.001$, and $p_c = 0.001$ and $A = 0.000135$ was set for the low-temperature value. The densities for the high-temperature set were initialized as before with $\rho_1^l = 6.287$ and $\rho_1^g = 1.425$. The low-temperature set is expected to be at a higher density ratio than the $\phi_1 = 729$ value obtained from the flat interface examples, due to the Laplace pressure in the bubble. Accordingly, the densities are initialized at $\rho_1^l = 12.0$ and $\rho_1^g = 0.012$ to account for the pressure difference. While this is also true for the high-temperature set, it was found that the time to reach equilibrium for the high-temperature set was much smaller than for the low and therefore, the difference was not accounted for.

The results for the high-temperature set are shown in Fig. 12 together with a sample spurious velocity field (this is the computed fluid velocity at steady state and should ideally be zero). The dashed lines are the fit of surface tension given by the Young-Laplace equation. The solid lines represents the average of the surface tension of each of the five results found by numerical integration of the normal and tangential parts of the pressure tensor given in Eq. (8). From Fig. 12 the surface tension from Young-Laplace's law and from integrating the pressure tensor are equal. The surface tensions computed by the two methods are in good agreement, and the linear relationship between bubble radius and the pressure difference is consistent with the Young-Laplace law.

In Fig. 13, the Young-Laplace test for the low-temperature set is shown, again with an example of the spurious velocities in one of the tests. As in the previous case, the values replicate the expected linear relationship between bubble radius and pressure difference. However, the surface tensions found by integrating the pressure tensor and from fitting are in slight disagreement. This was attributed to the thinness of the interface and error in the numerical integration and the computation of density profiles for thin interfaces. The average spurious velocities for all simulations of the Young-Laplace test are listed for the low-temperature set in Table I and the high-temperature set in Table II. Guo [36] reported spurious velocities that were $O(10^{-16})$. Here the average spurious velocities vary between $O(10^{-7})$ and $O(10^{-15})$. The higher spurious velocities in our simulations are attributed to the presence of two components rather than one.

In addition to characterizing spurious currents in the absence of flow, we also evaluate spurious currents with constant translation as in Wagner [34]. We consider a translation velocity $u_y^c = 0.001$ for the $\kappa = 0.001$ and $R_0 = 25$ cases in Tables I and II. The two simulations were run to 5×10^5 time steps. The results are shown in Fig. 14. Here Δu_y is the difference between the maximum y-component velocity and the average y-component velocity. For the high-temperature set, the steady state is $\Delta u_y = 1.3 \times 10^{-5}$, while for the low-temperature set it is $\Delta u_y = 4.4 \times 10^{-5}$.

When simulating curved interfaces using the interaction term, involving the interaction parameter A has caused increases in the surface tension when it is increased [46]. This is despite the fact that the interfacial terms in the free energy (3) are dependent on gradients of solvent only. We demonstrate that at high density ratios, the surface tension is practically unaffected by the interaction term. To do so we simulate

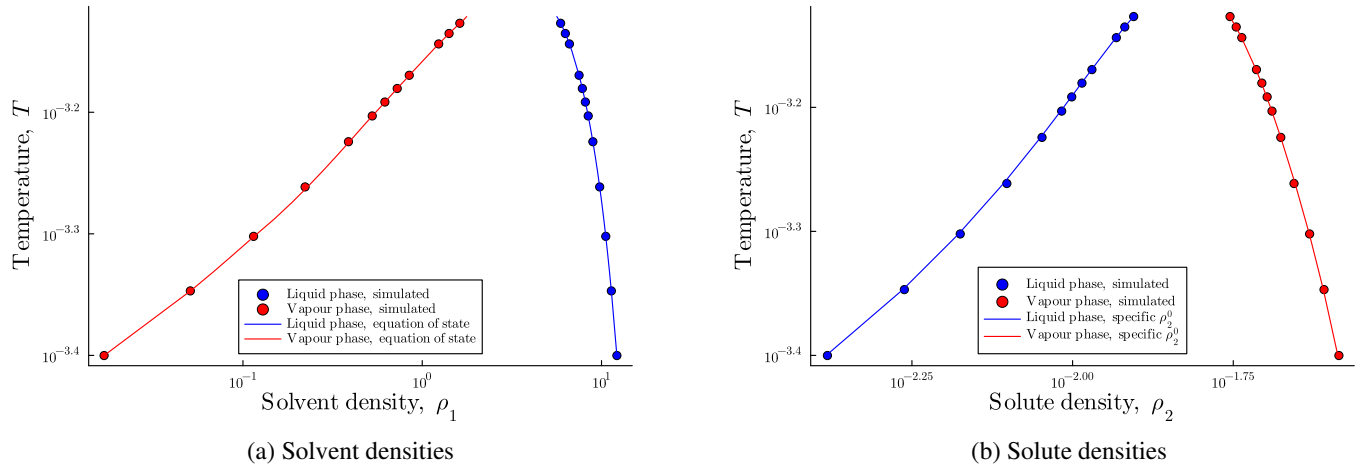


FIG. 9. High H equilibrium compositions of the phases for both components with $A = 0.00006$, $T_r \in [0.5, 0.92]$, and $p_c = 0.001$.

multiple Young-Laplace tests at both the high- and low-temperature sets for a range of A . The model parameters for each temperature set are the same as for the previous Young-Laplace tests.

Figure 15 shows the effect of the interaction strength A on surface tension. Multiple gas bubbles at select values of A were simulated at different initial radii $R_0 \in \{25, 28, 30, 32, 34\}$. The surface tension was calculated using the Young-Laplace law, and the results are shown in Fig. 15 for the high- and low-temperature parameters. As shown in Fig. 15, σ approximately doubles as A is increased by $100\times$. Simulations at high density ratios are unstable with higher values of A . We attribute this increase in surface tension to the changes in equilibrium composition of the solvent with increasing A (see Fig. 2), which causes a greater gradient in the solvent density between the liquid and vapor phases. Noticeable changes in σ occur when A is large enough that $H^{-1} \sim \phi_1$.

D. Solute mass transfer

In this last subsection, we demonstrate the mass transfer characteristics of the solute by calculating its diffusion coef-

ficient, D_2 , in the liquid phase of the solvent. The proposed free energy method allows such calculations to be performed in systems where topological changes also occur. Thus one can study mass transfer between bubbles/droplets and their surroundings in cases when the bubbles/droplets undergo coalescence or breakage.

The component mobility M_2 is directly specified in the model through the equilibrium. This results in the diffusion of chemical potential term on the right-hand side of Eq. (30b). We first show that Eq. (30b) can be written as a diffusion equation for ρ_2 in Appendix A. The resulting diffusion equation is given by Eq. (B5). Diffusion of the solute component exhibits the derived dependence on the mobility parameter Γ_2 , system temperature T , the average solute density ρ_2^0 , and the relaxation time τ_s . We note that the solvent mass equation can also be written as a diffusion equation and thus have a diffusion coefficient given by D_1 . The diffusion of each component will have a dependency on the other. However, we focus on D_2 because we are interested in the transport of the soluble gas; the solvent takes a secondary role as the medium through which the solute moves. The following test therefore uses a uniform solvent density distribution, and thus there is no influence due to

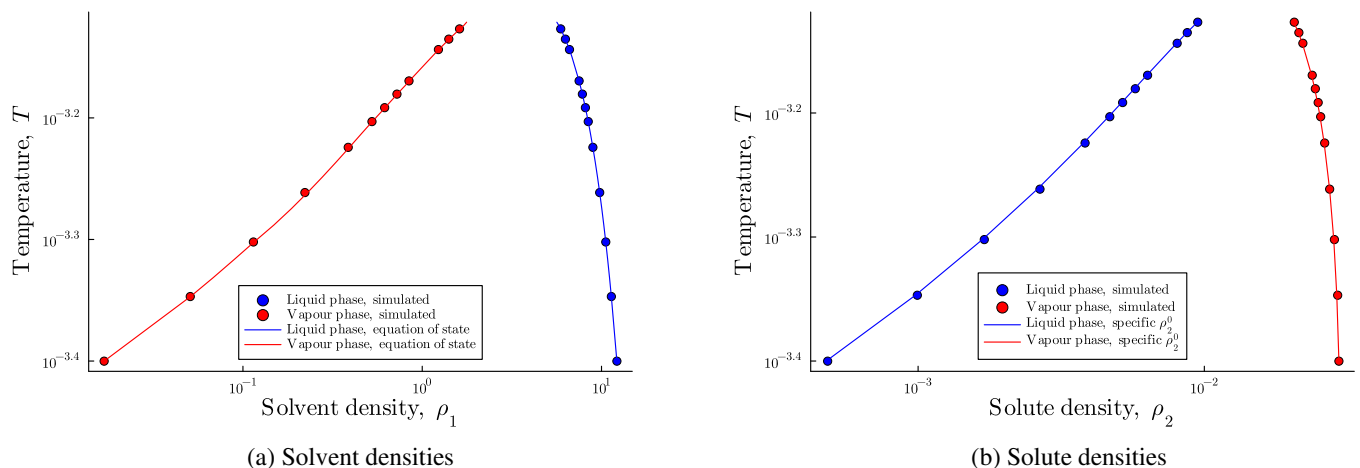


FIG. 10. Low H equilibrium compositions of the phases for both components with $A = 0.000135$, $T_r \in [0.5, 0.92]$, and $p_c = 0.001$.

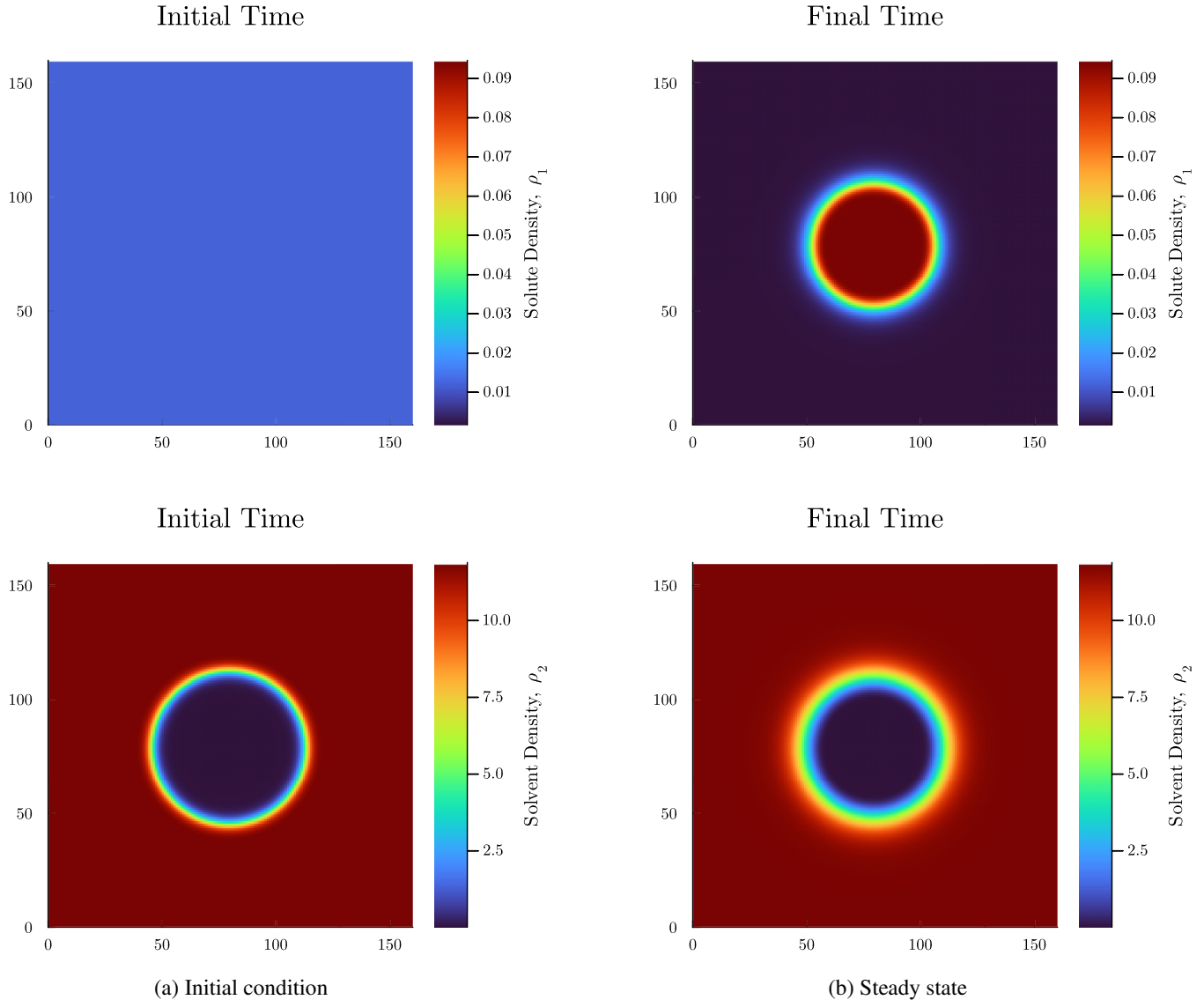


FIG. 11. Equilibrium density distributions for a bubble centered at $x = 80$ and $y = 80$ with $\kappa = 0.008$, $p_c = 0.01$, $T_r = 0.92$, and $A = 0.00125$.

minimal diffusion of solvent chemical potential or density for Eq. (30b).

To determine the diffusion coefficient numerically, we compute the decay of a sinusoidal density distribution given by

$$\rho_2(x_n) = \rho_2^0 + \rho_2^\epsilon \sin\left(\frac{2\pi(x_n - 1)}{N_x}\right), \quad (31)$$

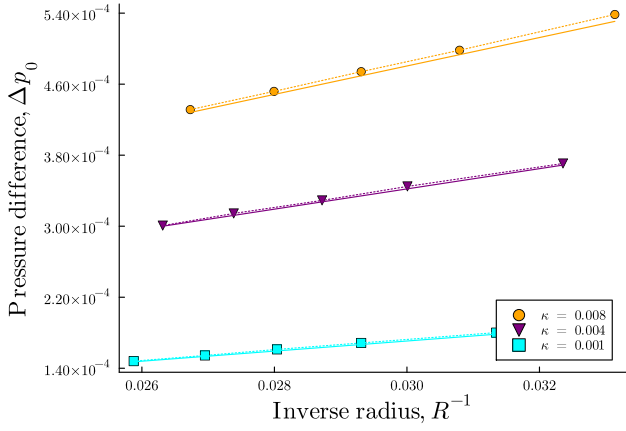
where $x_n = 1, 2, \dots, N_x$ is the node number in the x direction, ρ_2^ϵ is the initial amplitude of the perturbation, and ρ_2^0 is the average amount of solute. Since our interest is in the diffusion of the solute through the liquid phase of the solvent, the solvent is initialized at a constant value $\rho_1(x_n) = \rho_1^l$ corresponding to the liquid density as determined by the single component Maxwell construction. Keeping with the relation found in (17), the vapor branch is used to set the average amount of solute $\rho_2^0 \approx \rho_1^g$. The diffusion coefficient is determined by fitting the computed amplitude of the sinusoid with the analytical

solution

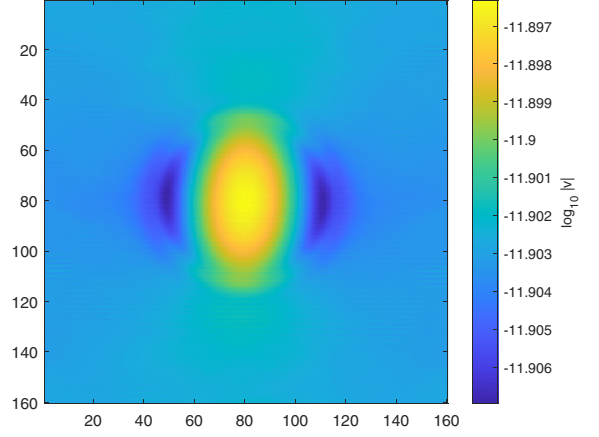
$$\rho_2^{\max}(t) = \rho_2^0 + \rho_2^\epsilon e^{-D_2 k^2 t}, \quad (32)$$

where $k = \frac{2\pi}{N_x}$.

These simulations were run to $t = 1 \times 10^5$ for $\Gamma_2 = 0.1$, $t = 5 \times 10^5$ for $\Gamma_2 = 0.01$, and $t = 6 \times 10^5$ for $\Gamma_2 = 0$ to ensure the sinusoidal perturbation decays sufficiently. The simulations were run using the low-temperature set with $\kappa = 0.008$, $A = 0.000135$, and $T_r = 0.5$ with both the relaxation time (and therefore also its viscosity) and mobility parameter varied to observe the effect on solute diffusion. When Γ_2 and τ_s were varied, the temperature was kept constant with $T = 0.000398$. τ_s was varied by changing the individual viscosities ν_1 and ν_2 . Keeping ν_2 constant at $\nu_2 = 0.033$, values of ν_1 were set at 0.133, 0.1 and 0.066. These viscosities correspond to τ_s values of approximately 0.9, 0.8 and 0.7, respectively. Due to the small solute density, τ_s is effectively insensitive to the value of ν_2 , and therefore ν_1 is varied. With



(a) Young-Laplace test



(b) Spurious velocities

FIG. 12. (a) Young-Laplace tests for the high-temperature set with the blue line referring to $\kappa = 0.008$, the purple line referring to $\kappa = 0.004$, and the orange line referring to $\kappa = 0.001$ with $A = 0.00135$ for all cases with initial radii given by $R_0 \in \{25, 28, 30, 32, 34\}$. (b) Spurious velocities for $R_0 = 30$ and $\kappa = 0.008$.

these values, the densities of the solvent in the vapor and liquid phases were $\rho_1^g = 0.0167$ and $\rho_1^l = 12.18$. Therefore the solvent was initialized at a constant value $\rho_1(x) = 12.0$. The solute was initialized with an average value $\rho_2^0 = 0.012$. The initial perturbation amplitude for all simulations was $\rho_2^\epsilon = 0.001$ which is 8.3% of the average. The resulting decays of the diffusing sinusoids for different relaxation times are shown for $\Gamma_2 = 0$ and $\Gamma_2 = 0.1$ in Fig. 16. The diffusion rate is only slightly changed by changing the relaxation time. It should be noted that for $\Gamma_2 = 0$ case, the diffusion terms do not appear and thus, the resulting diffusion is due to second-order error terms containing the forcing terms; this can be seen explicitly in Eq. (A19) in Appendix A.

The calculated values of the diffusion coefficient for a variety of relaxation times and temperatures are shown in Table III. They are compared to the expression derived in Appendix A. This expression contains the mobility coefficient,

Γ_2 , and other terms collected when expressing Eqs. (30) in terms of diffusion of component density rather than chemical potential. This expression is given by

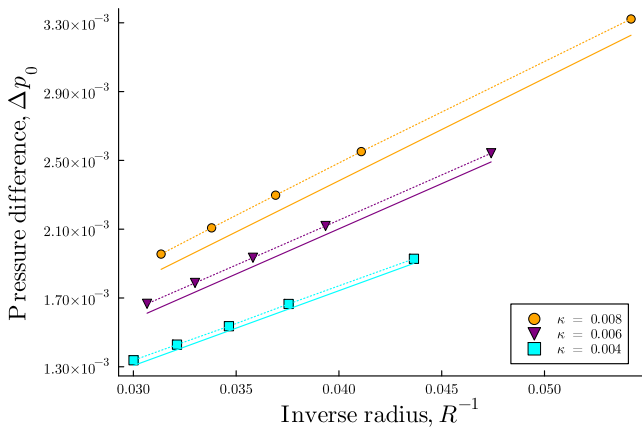
$$D_2 = R_2 T \left(\tau_s - \frac{\Delta t}{2} \right) \left(\frac{\Gamma_2}{\rho_2^0} + 1 \right). \quad (33)$$

In these simulations, the gas constant is set to unity, and the density ρ_1 can be substituted with ρ_1^l . It should be noted that some terms do not depend on the mobility coefficient. In the absence of these terms, this inherent diffusion of the solute is

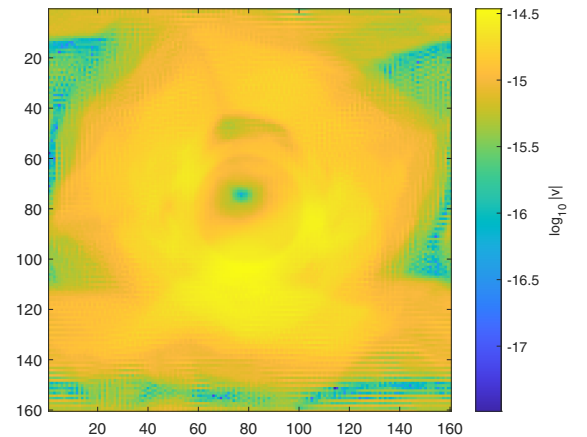
$$D_2^{\text{sys}} = R_2 T \left(\tau_s - \frac{\Delta t}{2} \right). \quad (34)$$

As previously stated, these terms are due to error terms in the forcing method.

The diffusion coefficients as predicted by this expression are given in Table IV, and they agree well with the numerically



(a) Young-Laplace test



(b) Spurious velocities

FIG. 13. (a) Young-Laplace tests for the low-temperature set with the blue line referring to $\kappa = 0.008$, the purple line referring to $\kappa = 0.006$, and the orange line referring to $\kappa = 0.004$ with $A = 0.000135$ for all cases with initial radii given by $R_0 \in \{25, 28, 30, 32, 34\}$. (b) Spurious velocities for $R_0 = 30$ and $\kappa = 0.008$.

TABLE I. Average spurious velocities for each Young-Laplace test presented in Fig. 12.

κ	25	28	30	32	34
R_0					
0.008	1.27×10^{-12}	1.27×10^{-12}	1.28×10^{-12}	1.28×10^{-12}	1.27×10^{-12}
0.004	1.24×10^{-12}	1.26×10^{-12}	1.27×10^{-12}	1.31×10^{-12}	1.31×10^{-12}
0.001	2.30×10^{-15}	9.51×10^{-15}	6.44×10^{-15}	8.62×10^{-15}	1.84×10^{-12}

determined values in Table III. There is a small discrepancy due to error terms that were neglected in the derivation of Eq. (33). However, it is evident that the introduction of the diffusion terms in the second moments allows for independent variation of the diffusion rate in the binary system.

V. CONCLUSIONS

In this paper, a model for describing the transport of a soluble gas in a nonideal solvent was presented. The two components are modeled using a combination of the ideal and Carnahan-Starling equations of state. A two-component version of the well-balanced [36] free energy lattice Boltzmann method [9] was developed to solve this system. We solve two lattice Boltzmann equations, with one for each component. The two LBEs are coupled through a term in the free energy and the use of a mixture velocity in the equilibrium distributions of both components. Use of the well-balanced approach minimizes discretization artifacts associated with the standard free energy LBM, which improves the thermodynamic consistency of the model. Diffusion of each component has been included by the introduction of mobility terms in the equilibrium distributions of each component. Equality of chemical potentials and pressures between the liquid and vapor phases separated by flat interfaces is shown, indicating that correct equilibrium has been reached.

Key model behavior such as phase separation, surface tension, and solute mass transfer were characterized. At the conditions we consider, the solvent densities in the vapor and liquid phases essentially follow the specified equation of state for the pure component (ignoring interaction with the solute). The soluble component distributes between the vapor and liquid phases of the solvent due to an interaction term in the free energy of the mixture. The soluble component obeys Henry's law, and Henry's constant depends on the interaction strength A . With increasing A , the amount of the solute gas that is dissolved in the liquid phase decreases. The solute partitions independent of the total amount of solute in the domain indicating that partitioning was dependent on A and thus the system's Henry's coefficient only. The free energy contains a term that only depends on gradients of solvent density but not solute density. This suggests that surface tension would be

independent of the solute density distribution. However, for both high and low reduced temperatures (high solvent density ratios) surface tension increases weakly with increasing A due to changes in the solvent density profile in the interface. We verified that the simulations are consistent with the Young-Laplace equation. The model is stable to at least a reduced temperature of 0.5, at which the solvent density ratio is 724, and a Henry's constant of 0.016. Therefore, simulations of common chemical systems at ambient conditions are possible. The rate of solute diffusion in the liquid phase of the solvent depends on the mixture's relaxation time, the solute mobility parameter, its gas constant, the system temperature, the solvent density, and the strength of the interaction between the components.

Overall, we have presented a diffuse interface model for simulation of systems with soluble gases in solvents that are present in liquid and vapor form. This means that simulations in which vapor-liquid interfaces undergo topological changes (i.e., coalescence and breakup of bubbles and droplets) are possible. The modeling approach will be applied next to systems with flow, such as rising and dissolving gas bubbles with deformation and breakup. The ability to simulate such systems is important to understanding a variety of engineering systems from micro-fluidic devices to large process equipment.

ACKNOWLEDGMENTS

C.B. thanks the Faculty of Science and Engineering at the University of Limerick for a scholarship that funded this research. The authors wish to acknowledge the Irish Centre for High-End Computing (ICHEC) for the provision of computational facilities and support. Some of the simulations were performed on the Luxembourg national supercomputer MeluXina. The authors gratefully acknowledge the LuxProvide teams for their expert support.

The authors have no conflicts of interest to disclose.

DATA AVAILABILITY

The data that support the findings of this article are not publicly available. The data are available from the authors upon reasonable request.

TABLE II. Average spurious velocities for each Young-Laplace test presented in Fig. 13.

κ	25	28	30	32	34
R_0					
0.008	3.32×10^{-15}	2.48×10^{-15}	1.68×10^{-13}	1.29×10^{-9}	3.43×10^{-15}
0.006	5.09×10^{-7}	2.75×10^{-15}	4.21×10^{-12}	1.7×10^{-11}	1.29×10^{-14}
0.004	3.253×10^{-15}	8.13×10^{-7}	1.19×10^{-15}	2.36×10^{-15}	1.28×10^{-15}

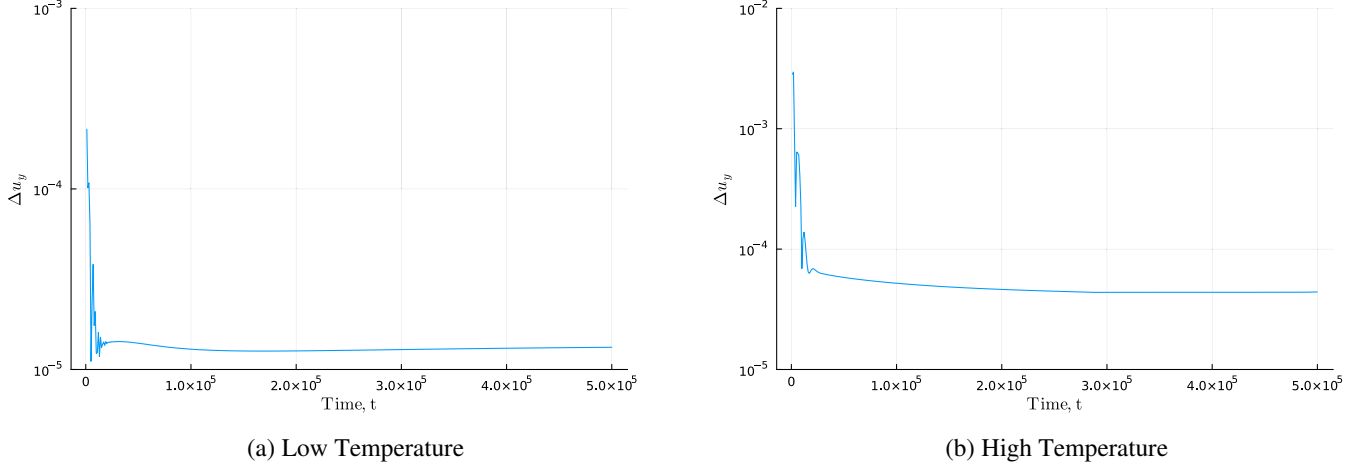


FIG. 14. Spurious currents with constant translation at a speed of $u_y^c = 0.001$. (a) Low-temperature case with $\kappa = 0.008$, $A = 0.000135$, and $R_0 = 25$. (b) High-temperature case with $\kappa = 0.008$, $A = 0.0000135$, and $R_0 = 25$.

APPENDIX A: CHAPMAN-ENSKOG ANALYSIS

Here we present the Chapman-Enskog analysis of the model. This will recover the Navier-Stokes equations from Eqs. (18a) and (18b). For convenience, these equations are

$$g_i(\mathbf{x} + \mathbf{c}_i \Delta t, t + \Delta t) = g_i(\mathbf{x}, t) - \frac{\Delta t}{\tau_s} [g_i(\mathbf{x}, t) - g_i^{\text{eq}}(\mathbf{x}, t)] + \left(1 - \frac{\Delta t}{2\tau_s}\right) G_i(\mathbf{x}, t) \Delta t, \quad (\text{A1a})$$

$$h_i(\mathbf{x} + \mathbf{c}_i \Delta t, t + \Delta t) = h_i(\mathbf{x}, t) - \frac{\Delta t}{\tau_s} [h_i(\mathbf{x}, t) - h_i^{\text{eq}}(\mathbf{x}, t)] + \left(1 - \frac{\Delta t}{2\tau_s}\right) H_i(\mathbf{x}, t) \Delta t, \quad (\text{A1b})$$

for the solvent and solute respectively. The moments of the equilibrium populations g_i^{eq} and h_i^{eq} satisfy

$$\sum_i g_i^{\text{eq}} = \rho_1, \quad (\text{A2a})$$

$$\sum_i g_i^{\text{eq}} c_{i\alpha} = \rho_1 u_\alpha, \quad (\text{A2b})$$

$$\sum_i g_i^{\text{eq}} c_{i\alpha} c_{i\beta} = \rho_1 u_\alpha u_\beta + (\Gamma_1 \mu_1) \delta_{\alpha\beta}, \quad (\text{A2c})$$

$$\sum_i g_i^{\text{eq}} c_{i\alpha} c_{i\beta} c_{i\gamma} = \rho_1 (u_\alpha \delta_{\beta\gamma} + u_\beta \delta_{\alpha\gamma} + u_\gamma \delta_{\alpha\beta}), \quad (\text{A2d})$$

for the solvent and

$$\sum_i h_i^{\text{eq}} = \rho_2, \quad (\text{A3a})$$

$$\sum_i h_i^{\text{eq}} c_{i\alpha} = \rho_2 u_\alpha, \quad (\text{A3b})$$

$$\sum_i h_i^{\text{eq}} c_{i\alpha} c_{i\beta} = \rho_2 u_\alpha u_\beta + (\Gamma_2 \mu_2) \delta_{\alpha\beta}, \quad (\text{A3c})$$

$$\sum_i h_i^{\text{eq}} c_{i\alpha} c_{i\beta} c_{i\gamma} = \rho_2 (u_\alpha \delta_{\beta\gamma} + u_\beta \delta_{\alpha\gamma} + u_\gamma \delta_{\alpha\beta}), \quad (\text{A3d})$$

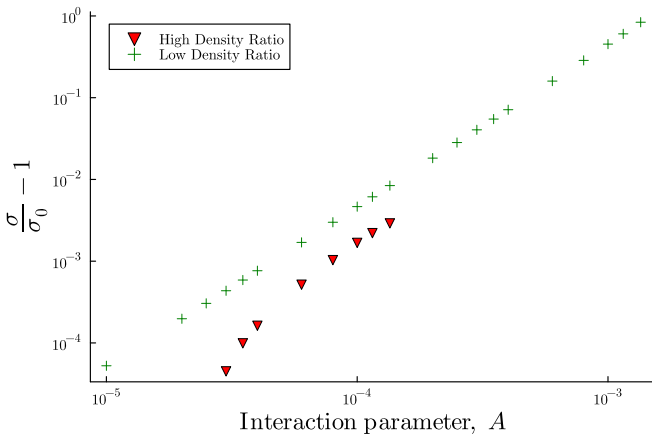


FIG. 15. Changes in surface tension with increasing A for the high-temperature value (with $\kappa = 0.008$, $T_r = 0.92$, and $p_c = 0.01$) and the low-temperature value (with $\kappa = 0.008$, $T_r = 0.5$, and $p_c = 0.001$). σ_0 is the value of σ when $A = 0$.

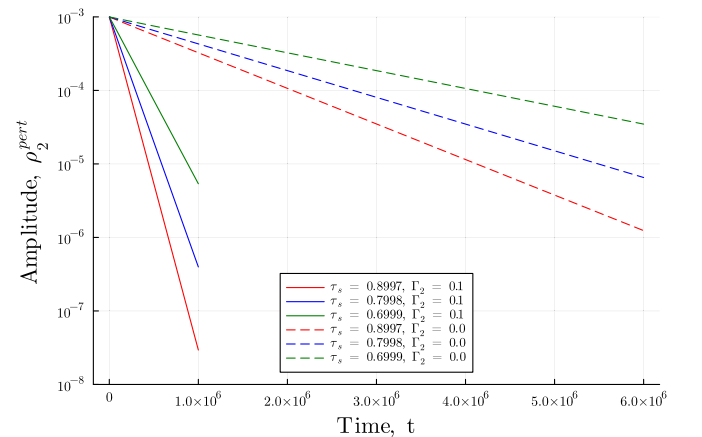


FIG. 16. Dependence of the diffusion coefficient on the relaxation time τ_s with $\Gamma_2 = 0$ (dashed lines) and $\Gamma_2 = 0.1$ (solid lines) for solute gas diffusion in the liquid phase.

TABLE III. Numerical solute diffusion constants D_2^{calc} for different relaxation times and mobilities.

τ_s	0.1	0.01	0
Γ_2			
0.9	0.0014872	0.0002920	0.0001591
0.8	0.0011168	0.0002192	0.0001193
0.7	0.0007458	0.0001463	0.0000796

for the solute. These are the zeroth, first, second, and third moments, respectively. The second moments contain both the standard well-balanced LBM term and an extra term to include diffusion for each component. The first moments, which define momentum, are coupled through a common velocity. This gives a total momentum ρu_α . This coupling allows derivation of a total momentum equation only, instead of separate momentum equation for each component. The total mass and momentum can be written in terms of the populations as

$$\rho = \rho_1 + \rho_2 = \sum_i (g_i + h_i), \quad (\text{A4a})$$

$$u_\alpha = \frac{1}{\rho} \sum_i \left(g_i c_{i\alpha} + \frac{\Delta t G_i c_{i\alpha}}{2} + h_i c_{i\alpha} + \frac{\Delta t H_i c_{i\alpha}}{2} \right). \quad (\text{A4b})$$

The force terms G_i and H_i in Eqs. (18a) and (18b) are given by the expressions

$$G_i = w_i \left(\frac{c_{i\alpha} (F_{1\alpha} + \Gamma_2 \partial_\alpha \mu_2)}{c_s^2} + \frac{B_{1\alpha\beta} (c_{i\alpha} c_{i\beta} - c_s^2 \delta_{\alpha\beta})}{c_s^4} \right), \quad (\text{A5a})$$

$$H_i = w_i \left(\frac{c_{i\alpha} (F_{2\alpha} + \Gamma_1 \partial_\alpha \mu_1)}{c_s^2} + \frac{B_{2\alpha\beta} (c_{i\alpha} c_{i\beta} - c_s^2 \delta_{\alpha\beta})}{c_s^4} \right), \quad (\text{A5b})$$

where

$$B_{1\alpha\beta} = u_\alpha (F_{1\beta} + \Gamma_2 \partial_\beta \mu_2 + c_s^2 \partial_\beta \rho_1) + \frac{1}{2} c_s^2 (u_\gamma \partial_\gamma \rho_1) \delta_{\alpha\beta}, \quad (\text{A6a})$$

$$B_{2\alpha\beta} = u_\alpha (F_{2\beta} + \Gamma_1 \partial_\beta \mu_1 + c_s^2 \partial_\beta \rho_2) + \frac{1}{2} c_s^2 (u_\gamma \partial_\gamma \rho_2) \delta_{\alpha\beta}. \quad (\text{A6b})$$

TABLE IV. Solute diffusion constants D_2 calculated by (33) for different relaxation times and mobilities.

τ_s	0.1	0.01	0
Γ_2			
0.9	0.0014850	0.0002917	0.0001588
0.8	0.0011138	0.0002188	0.0001193
0.7	0.0007427	0.0001459	0.0000796

These forcing terms have moments given by

$$\sum_i G_i = 0, \quad (\text{A7a})$$

$$\sum_i G_i c_i \alpha = F_{1\alpha} + \Gamma_2 \partial_\alpha \mu_2, \quad (\text{A7b})$$

$$\sum_i G_i c_i \alpha c_i \beta = \overline{B}_{1\alpha\beta} = B_{1\alpha\beta} + B_{1\beta\alpha}, \quad (\text{A7c})$$

and

$$\sum_i H_i = 0, \quad (\text{A8a})$$

$$\sum_i H_i c_i \alpha = F_{2\alpha} + \Gamma_1 \partial_\alpha \mu_1, \quad (\text{A8b})$$

$$\sum_i H_i c_i \alpha c_i \beta = \overline{B}_{2\alpha\beta} = B_{2\alpha\beta} + B_{2\beta\alpha}. \quad (\text{A8c})$$

To derive the corresponding Navier-Stokes equations, the populations g_i and h_i are Taylor expanded giving

$$D_i g_i + \frac{\Delta t}{2} D_i^2 g_i = -\frac{1}{\tau_s} (g_i - g_i^{\text{eq}}) + \left(1 - \frac{\Delta t}{2\tau_s}\right) G_i, \quad (\text{A9a})$$

$$D_i h_i + \frac{\Delta t}{2} D_i^2 h_i = -\frac{1}{\tau_s} (h_i - h_i^{\text{eq}}) + \left(1 - \frac{\Delta t}{2\tau_s}\right) H_i, \quad (\text{A9b})$$

where the operator on the left is $D_i = (\partial_t + c_{i\alpha} \partial_\alpha)$. To perform the Chapman-Enskog expansion, the populations, derivatives, and forcing terms are expanded in order of the Knudsen number, ϵ . These expansions read

$$g_i = g_i^{(0)} + \epsilon g_i^{(1)} + \epsilon^2 g_i^{(2)}, \quad \partial_\alpha = \epsilon \partial_\alpha^{(1)}, \quad (\text{A10a})$$

$$\partial_t = \epsilon \partial_{t_1} + \epsilon^2 \partial_{t_2}, \quad G_i = \epsilon G_i^{(1)}, \quad (\text{A10a})$$

$$h_i = h_i^{(0)} + \epsilon h_i^{(1)} + \epsilon^2 h_i^{(2)}, \quad \partial_\alpha = \epsilon \partial_\alpha^{(1)}, \quad (\text{A10b})$$

$$\partial_t = \epsilon \partial_{t_1} + \epsilon^2 \partial_{t_2}, \quad H_i = \epsilon H_i^{(1)}, \quad (\text{A10b})$$

where terms have been taken up to first or second order in ϵ . Applying these expansions to Eqs. (A9a) and (A9b) and collecting terms of different orders gives

$$\epsilon^0 : g_i^{(0)} = g_i^{\text{eq}}, \quad (\text{A11a})$$

$$\epsilon^1 : D_i^{(1)} g_i^{(0)} = -\frac{1}{\tau_s} g_i^{(1)} + \left(1 - \frac{\Delta t}{2\tau_s}\right) G_i^{(1)}, \quad (\text{A11b})$$

$$\epsilon^2 : \partial_{t_2} g_i^{(0)} + D_i^{(1)} g_i^{(1)} + \frac{\Delta t}{2} [D_i^{(1)}]^2 g_i^{(0)} = -\frac{1}{\tau_s} g_i^{(2)}. \quad (\text{A11c})$$

Similarly collecting terms for (A9b) gives

$$\epsilon^0 : h_i^{(0)} = h_i^{\text{eq}}, \quad (\text{A12a})$$

$$\epsilon^1 : D_i^{(1)} h_i^{(0)} = -\frac{1}{\tau_s} h_i^{(1)} + \left(1 - \frac{\Delta t}{2\tau_s}\right) H_i^{(1)}, \quad (\text{A12b})$$

$$\epsilon^2 : \partial_{t_2} h_i^{(0)} + D_i^{(1)} h_i^{(1)} + \frac{\Delta t}{2} [D_i^{(1)}]^2 h_i^{(0)} = -\frac{1}{\tau_s} h_i^{(2)}. \quad (\text{A12c})$$

The zeroth, first, and second moments of these equations are taken to derive the mass and momentum equations of each component. In the next sections, we will first derive the two mass equations followed by the total momentum equation.

1. Mass equations

The mass equations are derived by taking the zeroth moments of Eqs. (A11) and (A12) up to ϵ^2 , recursively solving at each order and adding each contribution up to order ϵ^2 . Inserting the definitions of g_i^{eq} and h_i^{eq} into the zeroth moments of Eqs. (A11a) and (A12a) leads to the following relations

$$\sum_i g_i^{(k)} = 0, \quad k \geq 1, \quad (\text{A13a})$$

$$\sum_i h_i^{(k)} = 0, \quad k \geq 1 \quad (\text{A13b})$$

for the the zeroth moments of the order ϵ^0 equations. The zeroth moment of the ϵ^1 equations given by Eq. (A11b) and Eq. (A12b) can be easily calculated giving

$$D_i^{(1)} g_i^{(0)} = \partial_{t_1} \rho_1 + \partial_\alpha^{(1)} (\rho_1 u_\alpha) = 0, \quad (\text{A14a})$$

$$D_i^{(1)} h_i^{(0)} = \partial_{t_1} \rho_2 + \partial_\alpha^{(1)} (\rho_2 u_\alpha) = 0. \quad (\text{A14b})$$

Lastly, the zeroth moments of the ϵ^2 equations need to be derived. The zeroth moments of (A11c) and (A12c) are

$$\sum_i \left\{ \partial_{t_2} g_i^{(0)} + D_i^{(1)} \left[\left(1 - \frac{\Delta t}{2\tau_s} \right) \left(g_i^{(1)} + \frac{\Delta t}{2} G_i^{(1)} \right) \right] \right\} = 0, \quad (\text{A15a})$$

$$\sum_i \left\{ \partial_{t_2} h_i^{(0)} + D_i^{(1)} \left[\left(1 - \frac{\Delta t}{2\tau_s} \right) \left(h_i^{(1)} + \frac{\Delta t}{2} H_i^{(1)} \right) \right] \right\} = 0. \quad (\text{A15b})$$

where (A11b) and (A12b) have been substituted into (A11c) and (A12c), respectively. Using Eqs. (A11b) and (A12b) again in (A15) results in

$$\begin{aligned} & \sum_i \left\{ \partial_{t_2} g_i^{(0)} + D_i^{(1)} \left[\left(1 - \frac{\Delta t}{2\tau_s} \right) \left(g_i^{(1)} + \frac{\Delta t}{2} G_i^{(1)} \right) \right] \right\} \\ &= \partial_{t_2} \rho_1 + \sum_i D_i^{(1)} \left[\left(\tau_s - \frac{\Delta t}{2} \right) \left(-D_i^{(1)} g_i^{(0)} + G_i^{(1)} \right) \right], \end{aligned} \quad (\text{A16a})$$

$$\begin{aligned} & \sum_i \left\{ \partial_{t_2} h_i^{(0)} + D_i^{(1)} \left[\left(1 - \frac{\Delta t}{2\tau_s} \right) \left(h_i^{(1)} + \frac{\Delta t}{2} G_i^{(1)} \right) \right] \right\} \\ &= \partial_{t_2} \rho_2 + \sum_i D_i^{(1)} \left[\left(\tau_s - \frac{\Delta t}{2} \right) \left(-D_i^{(1)} h_i^{(0)} + H_i^{(1)} \right) \right]. \end{aligned} \quad (\text{A16b})$$

Inserting the definition of D_i into Eq. (A16), each part of the second term on the right gives

$$\begin{aligned} & D_i^{(1)} \left[\left(\tau_s - \frac{\Delta t}{2} \right) \left(D_i^{(1)} g_i^{(0)} \right) \right] \\ &= \partial_{t_1} \left[\left(\tau_s - \frac{\Delta t}{2} \right) \left(\partial_{t_1} g_i^{(0)} + 2c_i \alpha \partial_\alpha^{(1)} g_i^{(0)} \right) \right] \\ &+ \partial_\alpha^{(1)} \left[\left(\tau_s - \frac{\Delta t}{2} \right) \partial_\beta^{(1)} (c_i \alpha c_i \beta g_i^{(0)}) \right], \end{aligned} \quad (\text{A17a})$$

$$\begin{aligned} & D_i^{(1)} \left[\left(\tau_s - \frac{\Delta t}{2} \right) \left(D_i^{(1)} h_i^{(0)} \right) \right] \\ &= \partial_{t_1} \left[\left(\tau_s - \frac{\Delta t}{2} \right) \left(\partial_{t_1} h_i^{(0)} + 2c_i \alpha \partial_\alpha^{(1)} h_i^{(0)} \right) \right] \\ &+ \partial_\alpha^{(1)} \left[\left(\tau_s - \frac{\Delta t}{2} \right) \partial_\beta^{(1)} (c_i \alpha c_i \beta h_i^{(0)}) \right], \end{aligned} \quad (\text{A17b})$$

and

$$D_i^{(1)} \left[\left(\tau_s - \frac{\Delta t}{2} \right) \left(G_i^{(1)} \right) \right] = \left(\partial_{t_1} + c_i \alpha \partial_\alpha^{(1)} \right) \left(\tau_s - \frac{\Delta t}{2} \right) G_i^{(1)}, \quad (\text{A18a})$$

$$D_i^{(1)} \left[\left(\tau_s - \frac{\Delta t}{2} \right) \left(H_i^{(1)} \right) \right] = \left(\partial_{t_1} + c_i \alpha \partial_\alpha^{(1)} \right) \left(\tau_s - \frac{\Delta t}{2} \right) H_i^{(1)}. \quad (\text{A18b})$$

Using Eqs. (A14a) and (A14b) to switch the time derivatives to spatial derivatives and solving for the moments of $g_i^{(0)}$ and $h_i^{(0)}$, the ϵ^2 equations read

$$\begin{aligned} 0 &= \partial_{t_2} \rho_1 - \partial_\alpha^{(1)} \left[\left(\tau_s - \frac{\Delta t}{2} \right) \left(\partial_\beta^{(1)} (\Gamma_1 \mu_1) \delta_{\alpha\beta} \right. \right. \\ &\quad \left. \left. + \partial_\beta^{(1)} \rho_1 u_\alpha u_\beta - F_{1\alpha} - \Gamma_2 \partial_\alpha^{(1)} \mu_2 \right) \right] \\ &- \partial_{t_1} \left[\left(\tau_s - \frac{\Delta t}{2} \right) \partial_\alpha^{(1)} \rho_1 u_\alpha \right], \end{aligned} \quad (\text{A19a})$$

$$\begin{aligned} 0 &= \partial_{t_2} \rho_2 - \partial_\alpha^{(1)} \left[\left(\tau_s - \frac{\Delta t}{2} \right) \left(\partial_\beta^{(1)} (\Gamma_2 \mu_2) \delta_{\alpha\beta} + \partial_\beta^{(1)} \rho_2 u_\alpha u_\beta \right. \right. \\ &\quad \left. \left. - F_{2\alpha} - \Gamma_1 \partial_\alpha^{(1)} \mu_1 \right) \right] - \partial_{t_1} \left[\left(\tau_s - \frac{\Delta t}{2} \right) \partial_\alpha^{(1)} \rho_2 u_\alpha \right]. \end{aligned} \quad (\text{A19b})$$

Adding the ϵ^1 and ϵ^2 equations and rewriting in vector notation gives the mass equations up to second order

$$\begin{aligned} \partial_t \rho_1 + \nabla \cdot (\rho_1 \mathbf{u}) &= \nabla \cdot [M_1 \nabla \mu_1 - M_2 \nabla \mu_2] \\ &+ e_1(\rho_1, \mathbf{u}) + O(u^3), \end{aligned} \quad (\text{A20a})$$

$$\begin{aligned} \partial_t \rho_2 + \nabla \cdot (\rho_2 \mathbf{u}) &= \nabla \cdot [M_2 \nabla \mu_2 - M_1 \nabla \mu_1] \\ &+ e_1(\rho_2, \mathbf{u}) + O(u^3), \end{aligned} \quad (\text{A20b})$$

which includes an error term given by

$$\begin{aligned} e_1(\rho_j, \mathbf{u}) &= \epsilon^2 \partial_\alpha^{(1)} \left[\left(\tau_s - \frac{\Delta t}{2} \right) \left(\partial_\beta^{(1)} \rho_j u_\alpha u_\beta - F_{j\alpha} \right) \right] \\ &+ \epsilon^2 \partial_{t_1} \left[\left(\tau_s - \frac{\Delta t}{2} \right) \left(\partial_\alpha^{(1)} \rho_j u_\alpha \right) \right] \end{aligned} \quad (\text{A21})$$

and mobility coefficients defined by $M_j = (\tau_s - \frac{\Delta t}{2}) \Gamma_j$. Later, it will be shown that an individual momentum equation cannot be derived for this system. Therefore the error term cannot be canceled as in [9].

However, when the total mass equation is considered, the sum of the errors can be simplified by use of the ϵ^1 total

momentum Eq. (A26)

$$e'_1(\rho, \mathbf{u}) = \varepsilon^2 \left[\partial_\alpha^{(1)} \left(\tau_s - \frac{\Delta t}{2} \right) \right] (-\partial_{t_1} \rho u_\alpha) + \varepsilon^2 \left[\partial_{t_1} \left(\tau_s - \frac{\Delta t}{2} \right) \right] (\partial_\alpha^{(1)} \rho u_\alpha). \quad (\text{A22})$$

This gives the total density equation

$$\partial_t(\rho) + \nabla \cdot (\rho \mathbf{u}) = e'_1. \quad (\text{A23})$$

This error vanishes when τ_s is constant, i.e., when the components have the same viscosities.

2. Momentum equation

The momentum equation is derived by taking the first moments of (A11) and (A12) and applying the same procedure as for the mass equations. Applying the definitions of g^{eq} and h^{eq} into the zeroth moments of Eqs. (A11a) and (A12a), the following relations can be derived:

$$\sum_i \left(c_i \alpha h_i^{(1)} + \frac{\Delta t}{2} c_i \alpha H_i^{(1)} \right) = - \sum_i \left(c_i \alpha g_i^{(1)} + \frac{\Delta t}{2} c_i \alpha G_i^{(1)} \right), \quad (\text{A24a})$$

$$\sum_i c_i \alpha h_i^{(k)} = - \sum_i c_i \alpha g_i^{(k)}, \quad k \geq 2. \quad (\text{A24b})$$

The ϵ^1 equations are derived by taking the first moments of Eqs. (A11b) and (A12b), which gives

$$\sum_i D_i^{(1)} c_i \alpha g_i^{(0)} = - \frac{1}{\tau_s} c_i \alpha g_i^{(1)} + \left(1 - \frac{\Delta t}{2\tau_s} \right) c_i \alpha G_i^{(1)}, \quad (\text{A25a})$$

$$\sum_i D_i^{(1)} c_i \alpha h_i^{(0)} = - \frac{1}{\tau_s} c_i \alpha h_i^{(1)} + \left(1 - \frac{\Delta t}{2\tau_s} \right) c_i \alpha H_i^{(1)}. \quad (\text{A25b})$$

The last step is to find $P_{j\alpha\beta}^{(1)} + \frac{\Delta t}{2} \overline{B}_{j\alpha\beta}$. The derivation follows similar to the Appendix of [36]. Taking the second moments of Eqs. (A11b) and (A12b) gives

$$- \frac{1}{\tau_s} P_{1\alpha\beta}^{(1)} + \left(1 - \frac{\Delta t}{2\tau_s} \right) \overline{B}_{1\alpha\beta} = \sum_i D_i^{(1)} c_i \alpha c_i \beta g_i^{(0)} = \partial_{t_1} (\rho_1 u_\alpha u_\beta + (\Gamma_1 \mu_1) \delta_{\alpha\beta}) + \partial_\gamma^{(1)} (c_s^2 \rho_1 [\mathbf{uI}]_{\alpha\beta\gamma}), \quad (\text{A29a})$$

$$- \frac{1}{\tau_s} P_{2\alpha\beta}^{(1)} + \left(1 - \frac{\Delta t}{2\tau_s} \right) \overline{B}_{2\alpha\beta} = \sum_i D_i^{(1)} c_i \alpha c_i \beta h_i^{(0)} = \partial_{t_1} (\rho_2 u_\alpha u_\beta + (\Gamma_2 \mu_2) \delta_{\alpha\beta}) + \partial_\gamma^{(1)} (c_s^2 \rho_2 [\mathbf{uI}]_{\alpha\beta\gamma}), \quad (\text{A29b})$$

where we have used Eqs. (A2d) and (A3d), and $[\mathbf{uI}]_{\alpha\beta\gamma} = (u_\alpha \delta_{\beta\gamma} + u_\beta \delta_{\alpha\gamma} + u_\gamma \delta_{\alpha\beta})$. One can rewrite Eqs. (A6a) and (A6b) as

$$\overline{B}_{1\alpha\beta} = [\overline{\mathbf{uF}}_1]_{\alpha\beta} + [\overline{\mathbf{u}\nabla}(\Gamma_2 \mu_2)]_{\alpha\beta} + (\partial_\gamma^{(1)} \rho_1) (c_s^2 [\mathbf{uI}]_{\alpha\beta\gamma}), \quad (\text{A30a})$$

$$\overline{B}_{2\alpha\beta} = [\overline{\mathbf{uF}}_2]_{\alpha\beta} + [\overline{\mathbf{u}\nabla}(\Gamma_1 \mu_1)]_{\alpha\beta} + (\partial_\gamma^{(1)} \rho_2) (c_s^2 [\mathbf{uI}]_{\alpha\beta\gamma}), \quad (\text{A30b})$$

where $[\overline{\mathbf{u}\nabla}(\Gamma_j \mu_j)]_{\alpha\beta} = u_\alpha \partial_\beta^{(1)} (\Gamma_j \mu_j)$. Thus,

$$- \frac{1}{\tau_s} P_{1\alpha\beta}^{(1)} - \frac{\Delta t}{2\tau_s} \overline{B}_{1\alpha\beta} = \partial_{t_1} (\rho_1 u_\alpha u_\beta + (\Gamma_1 \mu_1) \delta_{\alpha\beta}) - [\overline{\mathbf{uF}}_1]_{\alpha\beta} - [\overline{\mathbf{u}\nabla}(\Gamma_1 \mu_1)]_{\alpha\beta} + c_s^2 \rho_1 \partial_\gamma^{(1)} ([\mathbf{uI}]_{\alpha\beta\gamma}), \quad (\text{A31a})$$

$$- \frac{1}{\tau_s} P_{2\alpha\beta}^{(1)} - \frac{\Delta t}{2\tau_s} \overline{B}_{2\alpha\beta} = \partial_{t_1} (\rho_2 u_\alpha u_\beta + (\Gamma_2 \mu_2) \delta_{\alpha\beta}) - [\overline{\mathbf{uF}}_2]_{\alpha\beta} - [\overline{\mathbf{u}\nabla}(\Gamma_2 \mu_2)]_{\alpha\beta} + c_s^2 \rho_2 \partial_\gamma^{(1)} ([\mathbf{uI}]_{\alpha\beta\gamma}). \quad (\text{A31b})$$

A consequence of the use of a mixture velocity u_α in the equilibrium is that Eq. (A24a) involves both components. Derivation of momentum equations for each component will have terms containing population densities at first order in ϵ . Considering this, Eqs. (A25a) and (A25b) are added together and simplified by application of Eq. (A24a) and the definitions of the moments to get a total momentum equation

$$\partial_{t_1} (\rho u_\alpha) + \partial_\beta^{(1)} (\rho u_\alpha u_\beta) = F_{1\alpha} + F_{2\alpha}. \quad (\text{A26})$$

One can rearrange Eq. (A26) by Eqs. (A14) and multiplying by u_α and using the product rule. Multiplying this rearranged expression and Eq. (A26) by u_α and using the product rule again results in

$$\partial_{t_1} \rho u_\alpha u_\beta + \partial_\gamma^{(1)} \rho u_\alpha u_\beta u_\gamma = [\overline{\mathbf{uF}}_1]_{\alpha\beta} + [\overline{\mathbf{uF}}_2]_{\alpha\beta}, \quad (\text{A27})$$

where $[\overline{\mathbf{uF}}_j]_{\alpha\beta} = u_\alpha F_{j\beta} + u_\beta F_{j\alpha}$. Taking the first moment of the order ϵ^2 equations and making use of $P_{1\alpha\beta}^{(1)} = \sum_i c_i \alpha c_i \beta g_i^{(1)}$, $P_{2\alpha\beta}^{(1)} = \sum_i c_i \alpha c_i \beta h_i^{(1)}$ and $\overline{B}_{j\alpha\beta} = B_{j\alpha\beta} + B_{j\beta\alpha}$ the second-order equations read

$$\partial_{t_2} (\rho_1 u_\alpha) + \partial_\beta^{(1)} \left[\left(1 - \frac{\Delta t}{2\tau_s} \right) \left(P_{1\alpha\beta}^{(1)} + \frac{\Delta t}{2} \overline{B}_{1\alpha\beta} \right) \right] = 0, \quad (\text{A28a})$$

$$\partial_{t_2} (\rho_2 u_\alpha) + \partial_\beta^{(1)} \left[\left(1 - \frac{\Delta t}{2\tau_s} \right) \left(P_{2\alpha\beta}^{(1)} + \frac{\Delta t}{2} \overline{B}_{2\alpha\beta} \right) \right] = 0. \quad (\text{A28b})$$

Adding Eqs. (A31a) and (A31b) and using Eq. (A27) gives

$$-\sum_{j=1}^2 \left(\frac{1}{\tau_s} P_{j\alpha\beta}^{(1)} + \frac{\Delta t}{2\tau_s} \overline{B_{j\alpha\beta}} \right) = -\partial_\gamma^{(1)}(\rho u_\alpha u_\beta u_\gamma) + c_s^2 \rho \partial_\gamma^{(1)}([\mathbf{u}\mathbf{I}]_{\alpha\beta\gamma}) + \partial_{t_1}(\Gamma_1 \mu_1 + \Gamma_2 \mu_2) \delta_{\alpha\beta} - [\overline{\mathbf{u}\nabla}(\Gamma_1 \mu_1)]_{\alpha\beta} - [\overline{\mathbf{u}\nabla}(\Gamma_2 \mu_2)]_{\alpha\beta}, \quad (\text{A32a})$$

$$\sum_{j=1}^2 \left(P_{j\alpha\beta}^{(1)} + \frac{\Delta t}{2} \overline{B_{j\alpha\beta}} \right) = -c_s^2 \tau_s \rho (\partial_\alpha^{(1)} u_\beta + \partial_\beta^{(1)} u_\alpha + \partial_\gamma^{(1)} u_\gamma \delta_{\alpha\beta}) + \tau_s E_{2\alpha\beta} + O(u^3), \quad (\text{A32b})$$

where

$$E_{2\alpha\beta} = \sum_j (-\varepsilon \partial_{t_1}(\Gamma_j \mu_j) \delta_{\alpha\beta} + \varepsilon [\overline{\mathbf{u}\nabla}(\Gamma_j \mu_j)]_{\alpha\beta}). \quad (\text{A33})$$

Therefore, Eqs. (A28a) and (A28b) can be added and written as

$$\partial_{t_2}(\rho u_\alpha) - \nabla_1 \cdot \sigma_{\alpha\beta}^{(1)} = 0, \quad (\text{A34})$$

where $\sigma_{\alpha\beta}^{(1)} = \rho v (\partial_\alpha^{(1)} u_\beta + \partial_\beta^{(1)} u_\alpha + \partial_\gamma^{(1)} u_\gamma \delta_{\alpha\beta}) + v E_{2\alpha\beta}$ and $v = c_s^2 (\tau_s - \frac{\Delta t}{2})$, where $\tau_s = \frac{\rho_1 v_1 + \rho_2 v_2}{\rho c_s^2} + \frac{\Delta t}{2}$.

After taking the first and second equations of order ϵ^1 and ϵ^2 and converting to vector notation, the total momentum equation, up to second order, reads

$$\begin{aligned} \partial_t(\rho \mathbf{u}) + \nabla \cdot (\rho \mathbf{u} \mathbf{u}) \\ = -\rho_1 \nabla \mu_1 - \rho_2 \nabla \mu_2 + \nabla \cdot [\rho v (\nabla \mathbf{u} + \nabla \mathbf{u}^T) \\ + (\nabla \cdot \mathbf{u}) \mathbf{I} + v \mathbf{E}_2] + O(u^3). \end{aligned} \quad (\text{A35})$$

The complementing mass equations for each component are given by

$$\begin{aligned} \partial_t \rho_1 + \nabla \cdot (\rho_1 \mathbf{u}) = \nabla \cdot (M_1 \nabla \mu_1 - M_2 \nabla \mu_2) + e_1(\rho_1, \mathbf{u}) \\ + O(u^3), \end{aligned} \quad (\text{A36a})$$

$$\begin{aligned} \partial_t \rho_2 + \nabla \cdot (\rho_2 \mathbf{u}) = \nabla \cdot (M_2 \nabla \mu_2 - M_1 \nabla \mu_1) + e_1(\rho_2, \mathbf{u}) \\ + O(u^3). \end{aligned} \quad (\text{A36b})$$

The error term e_1 is due to inclusion of the diffusion term in the second moment. It is analogous to the error found for advection-diffusion equations solved by the lattice Boltzmann method.

APPENDIX B: DERIVATION OF THE SOLUTE DIFFUSION COEFFICIENT

Here we derive the expression for the effective solute diffusion coefficient in (A36b) as used in Sec. IV D. The error term E_1 in Eqs. (A36a) and (A36b) contains an error proportional to the force applied that therefore must be considered. This forcing term in E_1 is $-\partial_\alpha F_{i\alpha} = \partial_\alpha(\rho_i \partial_\alpha \mu_i)$. Neglecting solvent chemical potential gradients and considering the error term E_1 gives a mass equation for the

solute of

$$\partial_t \rho_2 + \nabla \cdot (\rho_2 \mathbf{u}) = \nabla \cdot \left[\left(\tau_s - \frac{\Delta t}{2} \right) (\Gamma_2 \nabla \mu_2 + \rho_2 \nabla \mu_2) \right]. \quad (\text{B1})$$

For the test in Sec. IV D, the solvent is initialized as uniform, the system is single-phase (liquid), and therefore terms with gradients of ρ_1 are negligible. Inserting the definition for the chemical potential of the solute and simplifying gives

$$\begin{aligned} \partial_t \rho_2 + \nabla \cdot (\rho_2 \mathbf{u}) \\ = \nabla \cdot \left[\left(\tau_s - \frac{\Delta t}{2} \right) (\Gamma_2 + \rho_2) \nabla [R_2 T \log(\rho_2)] \right]. \end{aligned} \quad (\text{B2})$$

On the right, $\nabla \log \rho_2 = \rho_2^{-1} \nabla \rho_2$, and it follows that the diffusive flux \mathbf{j}_2 is

$$\begin{aligned} \mathbf{j}_2 &= \left(\tau_s - \frac{\Delta t}{2} \right) (\Gamma_2 + \rho_2) \nabla [R_2 T \log(\rho_2)], \\ &= R_2 T \left(\tau_s - \frac{\Delta t}{2} \right) \frac{(\Gamma_2 + \rho_2)}{\rho_2} \nabla \rho_2, \\ &= R_2 T \left(\tau_s - \frac{\Delta t}{2} \right) \left(\frac{\Gamma_2}{\rho_2} + 1 \right) \nabla \rho_2, \\ &\equiv D_2 \nabla \rho_2. \end{aligned} \quad (\text{B3})$$

If, as in Sec. IV D, we have small perturbations in ρ_2 of amplitude ρ_2^{ϵ} around a mean ρ_2^0 , then D_2 can be approximated as

$$D_2 = R_2 T \left(\tau_s - \frac{\Delta t}{2} \right) \left(\frac{\Gamma_2}{\rho_2^0} + 1 \right). \quad (\text{B4})$$

Then the mass equation for the solute is

$$\partial_t \rho_2 + \nabla \cdot (\rho_2 \mathbf{u}) = \nabla \cdot (D_2 \nabla \rho_2). \quad (\text{B5})$$

APPENDIX C: CONSEQUENCES OF ALTERNATIVE RELAXATION TIME FORMULATIONS

Here we discuss different options for the relaxation time in a two-component system in which forces are included using the [50] forcing scheme. We consider two possible approaches and explain why we did not select them.

Firstly, if one considers the same analysis as in Appendix A but with separate relaxation times for the two components, the

zeroth-order relations remain the same,

$$\sum_i \left(c_i \alpha h_i^{(1)} + \frac{\Delta t}{2} c_i \alpha H_i^{(1)} \right) = - \sum_i \left(c_i \alpha g_i^{(1)} + \frac{\Delta t}{2} c_i \alpha G_i^{(1)} \right) \quad (\text{C1a})$$

$$\sum_i c_i \alpha h_i^{(k)} = - \sum_i c_i \alpha g_i^{(k)}, \quad k \geq 2. \quad (\text{C1b})$$

The ϵ^1 equations are different, however. These now read

$$\sum_i D_i^{(1)} c_i \alpha g_i^{(0)} = - \frac{1}{\tau_1} c_i \alpha g_i^{(1)} + \left(1 - \frac{\Delta t}{2\tau_1} \right) c_i \alpha G_i^{(1)}, \quad (\text{C2a})$$

$$\sum_i D_i^{(1)} c_i \alpha h_i^{(0)} = - \frac{1}{\tau_2} c_i \alpha h_i^{(1)} + \left(1 - \frac{\Delta t}{2\tau_2} \right) c_i \alpha H_i^{(1)}, \quad (\text{C2b})$$

which do not provide the closure needed to form the required momentum equation at first order.

One option to provide the necessary closure is to use a density and relaxation time weighted equilibrium velocity [55]. In this case, the mixture velocity is calculated as

$$u_\alpha = \frac{\frac{\rho_1 u_{1\alpha}}{\tau_1} + \frac{\rho_2 u_{2\alpha}}{\tau_2}}{\frac{\rho_1}{\tau_1} + \frac{\rho_2}{\tau_2}}. \quad (\text{C3})$$

This leads to the zeroth-order momentum equations

$$\begin{aligned} \sum_i \frac{1}{\tau_2} \left(c_i \alpha h_i^{(1)} + \frac{\Delta t}{2} c_i \alpha H_i^{(1)} \right) \\ = - \sum_i \frac{1}{\tau_1} \left(c_i \alpha g_i^{(1)} + \frac{\Delta t}{2} c_i \alpha G_i^{(1)} \right), \end{aligned} \quad (\text{C4a})$$

$$\sum_i \frac{1}{\tau_2} c_i \alpha h_i^{(k)} = - \sum_i \frac{1}{\tau_1} c_i \alpha g_i^{(k)}, \quad k \geq 2. \quad (\text{C4b})$$

This provides closure together with (C2) to get the momentum equation

$$\partial_{t_1}(\rho u_\alpha) + \partial_\beta^{(1)}(\rho u_\alpha u_\beta) = F_{1\alpha} + F_{2\alpha}. \quad (\text{C5})$$

The issue with this approach arises when trying to derive the momentum equation at second order in ϵ . It is not possible to derive an expression with the form of $P_{j\alpha\beta}^{(1)} + \frac{\Delta t}{2} \overline{B}_{j\alpha\beta}$ as in (A32) due to the two relaxation times. Therefore, neither approach of using two relaxation times gives a useful result. This observation is consistent with [49].

The solution suggested in [49], and the one we take in this paper, is to use one mixture relaxation time as suggested in [48]. This allows closure of the system as demonstrated in Appendix A.

-
- [1] W. W. Bowley and G. L. Hammond, Controlling factors for oxygen transfer through bubbles, *Ind. Eng. Chem. Process. Des. Dev.* **17**, 2 (1978).
- [2] S. S. Patil, N. A. Deshmukh, and J. B. Joshi, Mass-transfer characteristics of surface aerators and gas-inducing impellers, *Ind. Eng. Chem. Res.* **43**, 2765 (2004).
- [3] J. E. Olsen, D. Dunnebieer, E. Davies, P. Skjetne, and J. Morud, Mass transfer between bubbles and seawater, *Chem. Eng. Sci.* **161**, 308 (2017).
- [4] M. D. L. Rubia, A. García-Abuín, D. Gómez-Díaz, and J. M. Navaza, Interfacial area and mass transfer in carbon dioxide absorption in TEA aqueous solutions in a bubble column reactor, *Chem. Eng. Process. Process Intensif.* **49**, 852 (2010).
- [5] V. R. Parameswaran, M. R. Gogate, B. G. Lee, and S. Lee, Mass transfer in the liquid phase methanol synthesis process, *Fuel Sci. Technol. Int.* **9**, 695 (1991).
- [6] K. Tsuchiya, H. Mikasa, and T. Saito, Absorption dynamics of CO₂ bubbles in a pressurized liquid flowing downward and its simulation in seawater, *Chem. Eng. Sci.* **52**, 4119 (1997).
- [7] T. Saito, T. Kajishima, K. Tsuchiya, and S. Kosugi, Mass transfer and structure of bubbly flows in a system of CO₂ disposal into the ocean by a gas-lift column, *Chem. Eng. Sci.* **54**, 4945 (1999).
- [8] J. Rodríguez and E. Amores, CFD modeling and experimental validation of an alkaline water electrolysis cell for hydrogen production, *Processes* **8**, 1634 (2020).
- [9] M. R. Swift, E. Orlandini, W. R. Osborn, and J. M. Yeomans, Lattice Boltzmann simulations of liquid-gas and binary fluid systems, *Phys. Rev. E* **54**, 5041 (1996).
- [10] K. S. Ridl and A. J. Wagner, Lattice Boltzmann simulation of mixtures with multicomponent van der Waals equation of state, *Phys. Rev. E* **98**, 043305 (2018).
- [11] L. Zheng, S. Zheng, and Q. Zhai, Reduction-consistent phase-field lattice Boltzmann equation for N immiscible incompressible fluids, *Phys. Rev. E* **101**, 043302 (2020).
- [12] X. Yuan, B. Shi, C. Zhan, and Z. Chai, A phase field based lattice Boltzmann model for multiphase flows involving N immiscible incompressible fluids, *Phys. Fluids* **34**, 023311 (2022).
- [13] M. Soomro, L. F. Ayala, C. Peng, and O. M. Ayala, Fugacity-based lattice Boltzmann method for multicomponent multiphase systems, *Phys. Rev. E* **107**, 015304 (2023).
- [14] T. Krüger, H. Kusumaatmaja, A. Kuzmin, O. Shardt, G. Silva, and E. Viggien, *The Lattice Boltzmann Method: Principles and Practice*, Graduate Texts in Physics (Springer International Publishing, Cham, 2016).
- [15] D. M. Anderson, G. B. McFadden, and A. A. Wheeler, Diffuse-interface methods in fluid mechanics, *Annu. Rev. Fluid Mech.* **30**, 139 (1998).
- [16] R. G. van der Sman and S. van der Graaf, Diffuse interface model of surfactant adsorption onto flat and droplet interfaces, *Rheol. Acta* **46**, 3 (2006).
- [17] R. G. Van Der Sman and M. B. Meinders, Analysis of improved lattice Boltzmann phase field method for soluble surfactants, *Comput. Phys. Commun.* **199**, 12 (2016).
- [18] H. Liu and Y. Zhang, Phase-field modeling droplet dynamics with soluble surfactants, *J. Comput. Phys.* **229**, 9166 (2010).
- [19] Y. Shi, G. H. Tang, L. H. Cheng, and H. Q. Shuang, An improved phase-field-based lattice Boltzmann model for droplet

- dynamics with soluble surfactant, *Comput. Fluids* **179**, 508 (2019).
- [20] A. Briant, A. Wagner, and J. Yeomans, Lattice Boltzmann simulations of contact line motion. I. Liquid-gas systems, *Phys. Rev. E* **69**, 031602 (2004).
- [21] R. Sadeghi, M. S. Shadloo, M. Hopp-Hirschler, A. Hadjadj, and U. Nieken, Three-dimensional lattice Boltzmann simulations of high density ratio two-phase flows in porous media, *Comput. Math. Appl.* **75**, 2445 (2018).
- [22] L. Hao and P. Cheng, Pore-scale simulations on relative permeabilities of porous media by lattice Boltzmann method, *Int. J. Heat Mass Transf.* **53**, 1908 (2010).
- [23] N. Takada, M. Masaki, T. Akio, and H. Shigeo, Simulation of bubble motion under gravity by lattice Boltzmann method, *J. Nucl. Sci. Technol.* **38**, 330 (2001).
- [24] O. J. Ronsin, D. Jang, H. J. Egelhaaf, C. J. Brabec, and J. Harting, A phase-field model for the evaporation of thin film mixtures, *Phys. Chem. Chem. Phys.* **22**, 6638 (2020).
- [25] H. Kusumaatmaja, A. Dupuis, and J. M. Yeomans, Lattice Boltzmann simulations of drop dynamics, *Math. Comput. Simul.* **72**, 160 (2006).
- [26] A. J. Wagner and C. M. Pooley, Interface width and bulk stability: Requirements for the simulation of deeply quenched liquid-gas systems., *Phys. Rev. E* **76**, 045702 (2007).
- [27] T. Inamuro, T. Ogata, S. Tajima, and N. Konishi, A lattice Boltzmann method for incompressible two-phase flows with large density differences, *J. Comput. Phys.* **198**, 628 (2004).
- [28] A. Banari, C. Janßen, S. T. Grilli, and M. Krafczyk, Efficient GPGPU implementation of a lattice Boltzmann model for multiphase flows with high density ratios, *Comput. Fluids* **93**, 1 (2014).
- [29] H. W. Zheng, C. Shu, and Y. T. Chew, A lattice Boltzmann model for multiphase flows with large density ratio, *J. Comput. Phys.* **218**, 353 (2006).
- [30] J. Y. Shao, C. Shu, H. B. Huang, and Y. T. Chew, Free-energy-based lattice Boltzmann model for the simulation of multiphase flows with density contrast, *Phys. Rev. E* **89**, 033309 (2014).
- [31] X. D. Niu, Y. Li, Y. R. Ma, M. F. Chen, X. Li, and Q. Z. Li, A mass-conserving multiphase lattice Boltzmann model for simulation of multiphase flows, *Phys. Fluids* **30**, 013302 (2018).
- [32] A. Mazloomi M, S. S. Chikatamarla, and I. V. Karlin, Entropic lattice Boltzmann method for multiphase flows, *Phys. Rev. Lett.* **114**, 174502 (2015).
- [33] T. Lee and C. Lin, A stable discretization of the lattice Boltzmann equation for simulation of incompressible two-phase flows at high density ratio, *J. Comput. Phys.* **206**, 16 (2005).
- [34] A. J. Wagner and Q. Li, Investigation of Galilean invariance of multi-phase lattice Boltzmann methods, *Physica A* **362**, 105 (2006).
- [35] C. M. Pooley and K. Furtado, Eliminating spurious velocities in the free-energy lattice Boltzmann method, *Phys. Rev. E* **77**, 046702 (2008).
- [36] Z. Guo, Well-balanced lattice Boltzmann model for two-phase systems, *Phys. Fluids* **33**, 031709 (2021).
- [37] P. Yuan and L. Schaefer, Equations of state in a lattice Boltzmann model, *Phys. Fluids* **18**, 042101 (2006).
- [38] M. Wöhrwag, C. Semperebon, A. Mazloomi Moqaddam, I. Karlin, and H. Kusumaatmaja, Ternary free-energy entropic lattice Boltzmann model with a high density ratio, *Phys. Rev. Lett.* **120**, 234501 (2018).
- [39] A. Kupershtokh, D. Medvedev, and D. Karpov, On equations of state in a lattice Boltzmann method, *Comput. Math. Appl.* **58**, 965 (2009).
- [40] A. Kupershtokh, D. Medvedev, and D. Karpov, Equation of state for nonattracting rigid spheres, *J. Chem. Phys.* **51**, 635 (1969).
- [41] J. Carrero-Mantilla, Simulation of the (vapor+liquid) equilibria of binary mixtures of benzene, cyclohexane, and hydrogen, *J. Chem. Thermodyn.* **40**, 271 (2008).
- [42] A. Alanazi, S. Bawazeer, M. Ali, A. Keshavarz, and H. Hoteit, Thermodynamic modeling of hydrogen-water systems with gas impurity at various conditions using cubic and PC-SAFT equations of state, *Energy Convers. Manage.: X* **15**, 100257 (2022).
- [43] T. García-Córdova, D. N. Justo-García, B. E. García-Flores, and F. García-Sánchez, Vapor-liquid equilibrium data for the nitrogen + dodecane system at temperatures from (344 to 593) K and at pressures up to 60 MPa, *J. Chem. Eng. Data* **56**, 1555 (2011).
- [44] M. H. H. Fechter, J. Koschack, and A. S. Braeue, Vapor-liquid equilibria of the systems 1-octanol/nitrogen and 1-octanol/oxygen at pressures from 3 to 9 MPa and temperatures up to 613 K—Measured in a microcapillary with Raman spectroscopy, *Fuel* **323**, 124352 (2022).
- [45] A. J. Wagner, Thermodynamic consistency of liquid-gas lattice Boltzmann simulations, *Phys. Rev. E* **74**, 056703 (2006).
- [46] G. I. Tóth and B. Kvamme, Analysis of Ginzburg-Landau-type models of surfactant-assisted liquid phase separation, *Phys. Rev. E* **91**, 032404 (2015).
- [47] S. Chen and G. D. Doolen, Lattice Boltzmann method for fluid flows, *Annu. Rev. Fluid Mech.* **30**, 329 (1998).
- [48] H. Otomo, C. Crouse, M. Dressler, D. M. Freed, I. Staroselsky, R. Zhang, and H. Chen, Multi-component lattice Boltzmann models for accurate simulation of flows with wide viscosity variation, *Comput. Fluids* **172**, 674 (2018).
- [49] Y. Zhao, G. G. Pereira, S. Kuang, and B. Shi, On a modified pseudopotential lattice Boltzmann model for multicomponent flows, *Appl. Math. Lett.* **114**, 106926 (2021).
- [50] Z. Guo, C. Zheng, and B. Shi, Discrete lattice effects on the forcing term in the lattice Boltzmann method, *Phys. Rev. E* **65**, 046308 (2002).
- [51] M. Patra and M. Karttunen, Stencils with isotropic discretization error for differential operators, *Numer. Methods Partial Differ. Equations* **22**, 936 (2006).
- [52] T. Anderberg, Gradient and smoothing stencils with isotropic discretization error, <https://simplicial.net/hanlon/papers/stencils.pdf> (2012).
- [53] T. Besard, C. Foket, and B. De Sutter, Effective extensible programming: Unleashing Julia on GPUs, *IEEE Trans. Parallel Distrib. Syst.* **30**, 827 (2018).
- [54] R. Sander, Compilation of Henry's law constants (version 4.0) for water as solvent, *Atmos. Chem. Phys.* **15**, 4399 (2015).
- [55] X. Shan and G. Doolen, Multicomponent lattice-Boltzmann model with interparticle interaction, *J. Stat. Phys.* **81**, 379 (1995).